Ore Geology Reviews 105 (2019) 404–422

Contents lists available at ScienceDirect

Ore Geology Reviews

journal homepage: www.elsevier.com/locate/oregeorev

Source of ore-forming fluids of the Yangshan gold field, western Qinling orogen, China: Evidence from microthermometry, noble gas isotopes and in situ sulfur isotopes of Au-carrying pyrite

Jinlong Liang[a], Jie Li[b,*], Weidong Sun[c,d,e], Jing Zhao[a], Wei Zhai[f,*], Yi Huang[a], Mingchun Song[g], Shijun Ni[a], Qirong Xiang[a], Jianchao Zhang[h], Jialong Hao[h], Zhenglu Nan[i], Jianzhong Li[i]

[a] Department of Geochemistry, Chengdu University of Technology, Chengdu 610059, China
[b] School of Resources, Hebei GEO University, Shijiazhuang 050031, China
[c] Center of Deep Sea Research, Institute of Oceanography, Chinese Academy of Sciences(CAS), Qingdao 266071, China
[d] Laboratory for Marine Mineral Resources, Qingdao National Laboratory for Marine Science and Technology, Qingdao 266237, China
[e] Center for Excellence in Tibetan Plateau Earth Sciences, CAS, Beijing 100101, China
[f] School of Marine Sciences, Sun Yat-Sen University, Guangzhou 510006, China
[g] Shandong Provincial Bureau of Geology and Mineral Resources, Jinan 250013, China
[h] Key Laboratory of Earth and Planetary Physics, Institute of Geology and Geophysics, CAS, Beijing 100029, China
[i] 12th Branch of Chinese Gold Armed Police Army, Chengdu 610036, China

ARTICLE INFO

Keywords:
Yangshan gold ore belt
Noble gas isotopes
NanoSIMS elemental mapping
Sulfur isotopes
Western Qinling orogen

ABSTRACT

The Yangshan gold ore belt contains a series of sediment-hosted disseminated gold deposits in the southern subzone of the western Qinling orogen. The ore deposits formed in the Middle Devonian carbonaceous clastic-carbonate sequences that underwent strong deformation and low greenschist facies regional metamorphism. The shapes and distribution of the ore bodies are strictly confined by the E-W-trending Anchanghe-Guanyinba thrust fault zone. Pyrite and arsenopyrite are the major Au-carrying minerals. Microthermometric results show that the ore-forming fluids are CO_2-rich aqueous solutions. The homogenization temperatures range from 221 to 303.5 °C, and salinities range from 2.0 to 7.2 wt% NaCl equiv. These characteristics are consistent with orogenic gold deposit. Noble gas isotopic measurement shows that $^3He/^4He$ ratios of pyrite and quartz grains inherited from the mineralized carbonaceous phyllite, ranging from 0.033 to 0.081 Ra, implying that the origins of ore fluids are restricted within the crustal regime. The $^{40}Ar/^{36}Ar$ ratios range from 434 to 863, indicating 34 to 68% crust-derived radiogenic $^{40}Ar^*$ in the ore fluids. Based on the backscattered electron (BSE) maps of pyrite, three generations (i.e. core, mantle, rim) are distinguished: pre-ore pyrite including framboidal pyrites and the cores of zoned pyrites both in the phyllite and plagiogranite dikes; ore stage pyrites including the middle zones of the three-zoned pyrites in the granitic dikes and the outer zones of the zoned pyrites in the phyllite; post-ore pyrites, i.e. the outermost rims of the zoned pyrites in the dikes. The arsenopyrite in the phyllite has similar texture to the pyrite, and is regarded as the peak of the mineralization due to its highest Au concentrations. High spatial resolution NanoSIMS multi-elemental maps of the pyrites reveal that (i) gold is distributed heterogeneously as lattice-bounded Au in the zoned pyrites with higher Au (As) in the middle zones and lower Au (As) in the inner and outermost zones. No nano-particles of native gold was identified in pyrite; (ii) gold mineralization occurred in a single event instead of multistage ore formation; (iii) gold precipitation event is followed by an overgrown zone with low Au and As concentrations. In situ sulfur isotopes of Au-bearing pyrite identified two types of sulfur sources: one is framboidal pyrite and the barren core of pyrite in the carbonaceous phyllite, which have very negative $\delta^{34}S$ values ($< -20\%$); the other is the Au-bearing overgrowth zone of pyrite both from the granitic dike and phyllite, which have higher $\delta^{34}S$ values ranging from -7.3 to 1.3%. This result indicates that the barren pyrites have the sulfur isotopic feature of reduction of seawater sulfate, whereas the As-, Au-bearing pyrites are likely derived from a magmatic sulfur contaminated by a sedimentary sulfur.

Combining Au concentrations with the corresponding $\delta^{34}S$ values in the pyrites reveals that the zones with high Au have lower $\delta^{34}S$ values (and vice versa). This coupling relation between Au and S isotope has been also identified in other orogenic and Carlin-type gold deposits. The oxidation of ore fluid is taken as the key for gold precipitation during formation of orogenic gold deposit. However, the oxidation of ore fluids accompanied by

* Corresponding authors.
E-mail addresses: lijiesue@163.com (J. Li), eeszw@mail.sysu.edu.cn (W. Zhai).

https://doi.org/10.1016/j.oregeorev.2018.12.029
Received 17 January 2018; Received in revised form 18 December 2018; Accepted 31 December 2018
Available online 02 January 2019
0169-1368/

the escape of reduced gas (e.g. H_2S) should result in high Au coupled with high $\delta^{34}S$. Therefore, we propose that the Yangshan gold deposit forms through partitioning aqueous vapor with high Au, As, and lower $\delta^{34}S$ from a deep magma chamber under the ore field, which leads to overgrowth of the pre-existing pyrites.

Based on the geological features, texture of pyrite, and sulfur isotopic characteristics, we suggested that the Yangshan gold deposits have the characteristics between Carlin-type and orogenic gold deposits. They are the product of the western Qinling orogeny during the Late Triassic.

1. Introduction

Most of the sediment-hosted gold deposits have been regarded as orogenic ones, especially, those developed in collisional orogens, or accretionary crustal margins (Groves et al., 1998; Goldfarb and Groves, 2015 and references therein). These gold deposits commonly occurred in slightly metamorphic terrances, controlled by faults, and displayed as sulfide-quartz veins or stockworks with visible native gold (Goldfarb and Groves, 2015 and references therein). Although orogenic gold deposits have been emphasized to be the product of metamorphic devolatilization during orogenesis or subduction, the hypotheses of multiple fluid resources including metamorphic fluids derived from dewatering of supracrustal rocks (Phillips and Groves, 1983; Phillips and Powell, 2009), meteoric water (Hagemann et al., 1994), magmatic hydrothermal fluids (Mueller et al., 2008; Robert, 2001), lower crustal or mantle fluids (Hronsky et al., 2012; Goleby et al., 2004) etc., have been suggested (Goldfarb and Groves, 2015 and references therein). It is well known that HS^- is the principal ligand responsible for Au transport under reduced conditions (Hofstra et al., 1991; Stenger et al., 1998; Hofstra and Cline, 2000; Cline et al., 2005; Loucks and Mavrogenes, 1999). Therefore, it is the key to correctly characterize the nature of ore-forming fluids and identify sulfur sources for understanding the formation of sediment-hosted gold deposits. To resolve the controversy of ore fluid resources, trace elements of pyrite have been applied for the past decade (Large et al., 2009, 2011), which utilized the technique of LA-ICP-MS to characterize the trace elemental maps of ore-related pyrite, and further elucidate the ore fluids evolution and gold precipitation. Simultaneously, in situ sulfur isotopes analyses of pyrites using SIMS, NanoSIMS or SHRIMP overcame the shortcomings of mixed sulfur resources and ambiguous interpretation of fluid resources (Kesler et al., 2005; Chang et al., 2008; Barker et al., 2009; Hou et al., 2016; Ma et al., 2018; Yan et al., 2018; Zhao et al., 2018). Recent years saw an innovative application of multiple sulfur isotopic tracers combined mass dependent fractionation ($\delta^{34}S$) with mass independent fractionation ($\Delta^{33}S$) to monitor the fluid resources and evolution, especially, for those orogenic gold deposits hosted in the Archean sedimentary rocks (Xue et al., 2013; Selvaraja et al., 2017a, b; Laflamme et al., 2017).

The sediment-hosted gold deposits in the western Qinling orogen, China, were classified into two types, i.e. orogenic ones in the northern Qinling orogen, and Carlin-like ones in the southern Qinling orogen

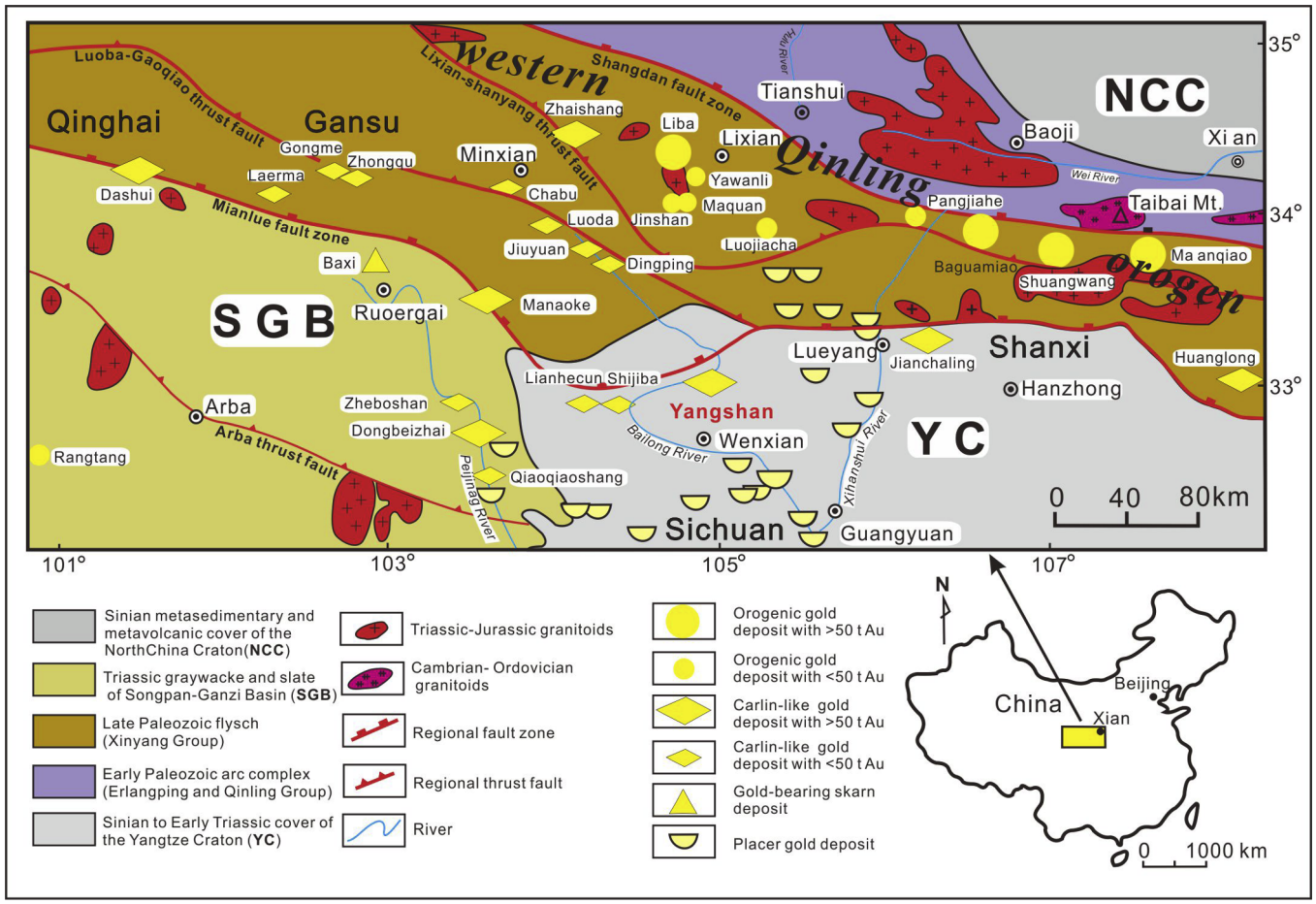

Fig. 1. Simplified geological map of the western Qinling orogen (after Mao et al., 2002) shows the major lithological units, fault zones and distribution of the Carlin-like, orogenic, skarn, and placer gold deposits (NCC-North China craton; YC- Yangtze craton, SGB-Songpan-Ganzi basin).

(Mao et al., 2002, Chen et al., 2004). A recent study proposed that ore fluids and metals may be derived from a deep magmatic source in the southern Qinling, while the ore-forming materials may originate from metamorphism of the underlying SEDEX sequences in the northern Qinling (Ma et al., 2018). The Yangshan gold field is a representative disseminated sediment-hosted ore belt in the southern Qinling. Since it was discovered ten years ago, studies of deposit geology (Yan et al., 2008, 2010), mineralogy (Liang et al., 2013, 2014), geochemistry (Ding et al., 2014; Li et al., 2014; Yang et al., 2016; Zhao et al., 2016), fluid inclusion (Li et al., 2007a), and geochronology (Qi et al., 2005; Yang et al., 2006) have been conducted. Some mineral systems models, such as orogenic, Carlin-type or Carlin-like, and epizonal styles etc. have been proposed (Liang et al., 2013, 2014; Li et al., 2014; Yang et al., 2016). However, the nature, origin of ore fluids, genetic mechanism and metallogenic type for the Yangshan gold deposits remain poorly understood.

In this paper, we present data sets of microthermometry, He-Ar isotopes of fluid inclusions, multi-element maps, and in-situ sulfur isotopes of Au-bearing arsenian pyrite of the Yangshan gold deposits using high spatial resolution NanoSIMS, try to address where the Au-carrying fluids came from, and what was the mechanism that triggered Au precipitation from the hydrothermal fluid. On this basis, we proposed a model suitable to the disseminated sediment-hosted gold deposits in the southern subzone of the western Qinling orogen.

2. Regional geology and deposit geology of the Yangshan gold ore field

2.1. Regional geological setting

The present geologic framework of the western Qinling orogen is the result of convergence and closure of two paleo-oceanic basins, i.e. the Shangdan Ocean and the Mianlue Ocean between the Yangtze craton (YC), Qinling micro-continental block, and the North China craton (NCC) from the south to the north during the Middle Devonian to the Early Carboniferous, which was summarized as the three-plate plus two-suture tectonic framework (Meng and Zhang, 2000; Zhang et al., 2004a) (Fig. 1). The northern Shangdan Paleo-ocean and the southern Mianlue Paleo-ocean closed during the Late Carboniferous and the Middle Triassic respectively (Sun et al., 2002a; Sun et al., 2002b). Subsequently, the western Qinling region underwent a continent-continent collision causing orogenesis during the Middle Triassic to the Late Triassic, and extensional collapse during the Late Triassic to the Middle Jurassic (Li et al., 2014).

At present, the western Qinling orogen can be divided into three subzones by the Shangdan Suture (i.e. Shangdan thrust fault zone) and the Mianlue Suture (i.e. Mianlue thrust fault zone) (Fig. 1). The northern zone consists of an Early Paleozoic arc accreted to the NCC during the Late Silurian (Sun et al., 2002b). The central zone is dominated by clastic sequences that formed in a Late Paleozoic basin between the converging NCC and YC, and contains dozens of orogenic and Carlin-like gold deposits with the Lixian-Shanyang thrust fault between the two types as a limit (Fig. 1). The southern zone is characterized by metasedimentary rock of the Late Paleozoic Songpan-Ganzi Basin (SGB) (Liang et al., 2014) (Fig. 1). Since the 1980s, > 50 gold deposits have been discovered in the central zone, including some large deposits with over 50 t Au reserves, such as Dashui, Zhaishang, Jianchaling, Dongbeizhai, and Manaoke gold deposits (Fig. 1) (Chen et al., 2004; Ma et al., 2018; Zhang et al., 2000). The Yangshan gold belt is the largest sediment-hosted disseminated gold ore assemblage in the central zone, where the Mianlue thrust fault branch changes into a series of arc-shaped structures bending to the south, to form the so called Wenxian arcuate structure, which controls the occurrences of gold deposits in the belt (Fig. 1).

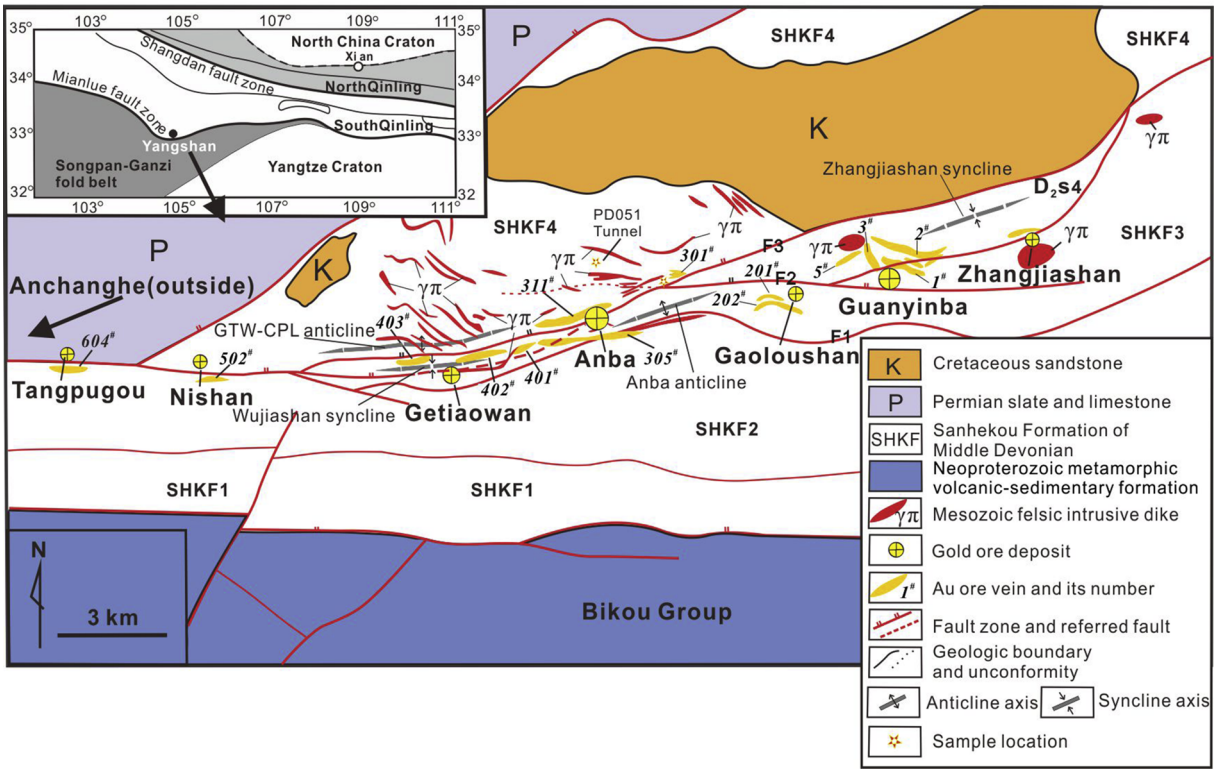

Fig. 2. Simplified geological map of the Yangshan gold ore belt (after Liang et al., 2014), shows the major lithological units, ore-controlling structures, and the four ore deposits of Getiaowan, Anba, Gaoloushan (namely Yangshan), and Guanyinba. No gold reserves have been evaluated for the Tangpugou, Nishan, and Zhangjiashan ore deposits at present.

2.2. Geology of the Yangshan gold deposits

The Middle Devonian Sanhekou Formation (SHKF), is the main host rock of the Yangshan gold deposits. It is composed of clastic-carbonate sedimentary sequences that have generally undergone low greenschist facies metamorphism and strong deformation. It consists of black-grey silty sandstone, sericite-phyllite, black shale with significant organic matter and thick bedded silicified limestone. The SHKF is divided into six lithological units (SHKF1-6). The third unit (SHKF3) is the favorable ore-hosting unit. It consists predominantly of thinly bedded sericitic and silty phyllite enriched in organic matter, with interlayered silicified limestone lenses (Fig. 2). The major and subordinate fault planes cut the ore-bearing lithological units to form sausage-shaped ore bodies in the horizontal plane (Fig. 3A). Drilling exploration showed the ore bodies commonly pinch out at a depth of less than one thousand meters (Fig. 3B).

In addition to the Devonian sedimentary rocks, there are Middle to Neoproterozoic metamorphosed volcanic-sedimentary sequences of the Bikou Group in the southern margin of the ore belt, a Permian sedimentary package on the northwestern margin, and thick bedded Jurassic sandstones unconformably overlying the Devonian sequences within the northeastern area (Fig. 2). All of these lithological units have nothing to do with Au mineralization. The Yangshan gold ore belt defined by the 30-km-long, E-W trending Anchanghe-Guanyinba fault zone, includes 7 ore deposits, i.e. Zhangjiashan, Guanyinba (also named Yangshan), Gaoloushan, Anba, Getiaowan, Nishan, and Tangpugou from east to west (Fig. 2). The current exploration work is focused on the middle four deposits of Guanyinba, Gaoloushan, Anba, and Getiaowan. Of these, the Anba deposit contains a significant fraction of the total Au reserves.

The Anchanghe-Guanyinba fault is the main ore-controlling structure, which is a branch of the regional Mianlue fault zone. It has a variable width from tens of meters to several kilometers (Fig. 2). The fault predominantly dips to the north, occasionally to the south, with a dip angle from 50 to 70°. The fault plane is commonly parallel to the foliation of the Middle Devonian phyllitic country rocks. The fault zone locally includes three offset branches namely F1, F2, and F3, dipping to the south, north, and south respectively, which control the different mineralized vein groups within the Anba and Getiaowan deposits (Fig. 2).

The near E-W trending Getiaowan-Caopingliang (GTW-CPL) anticline is the largest fold in the gold belt with a width of 1 km, extends about 10 km, and is parallel to the main structural lineaments (Fig. 2). At the Anba gold deposit, both north and south limbs of the anticline are exposed, whereas the south limb is cut off by the Anchanghe-Guanyinba fault at the Getiaowan gold deposit. The Middle Devonian metasedimentary SHKF constitutes the two limbs and core of the anticline. The core of the fold controls the location of No. 301 ore vein group (Fig. 2). The Wujiashan syncline and Zhangjiashan syncline located to the south of the GTW-CPL anticline, are the major synclines in the gold

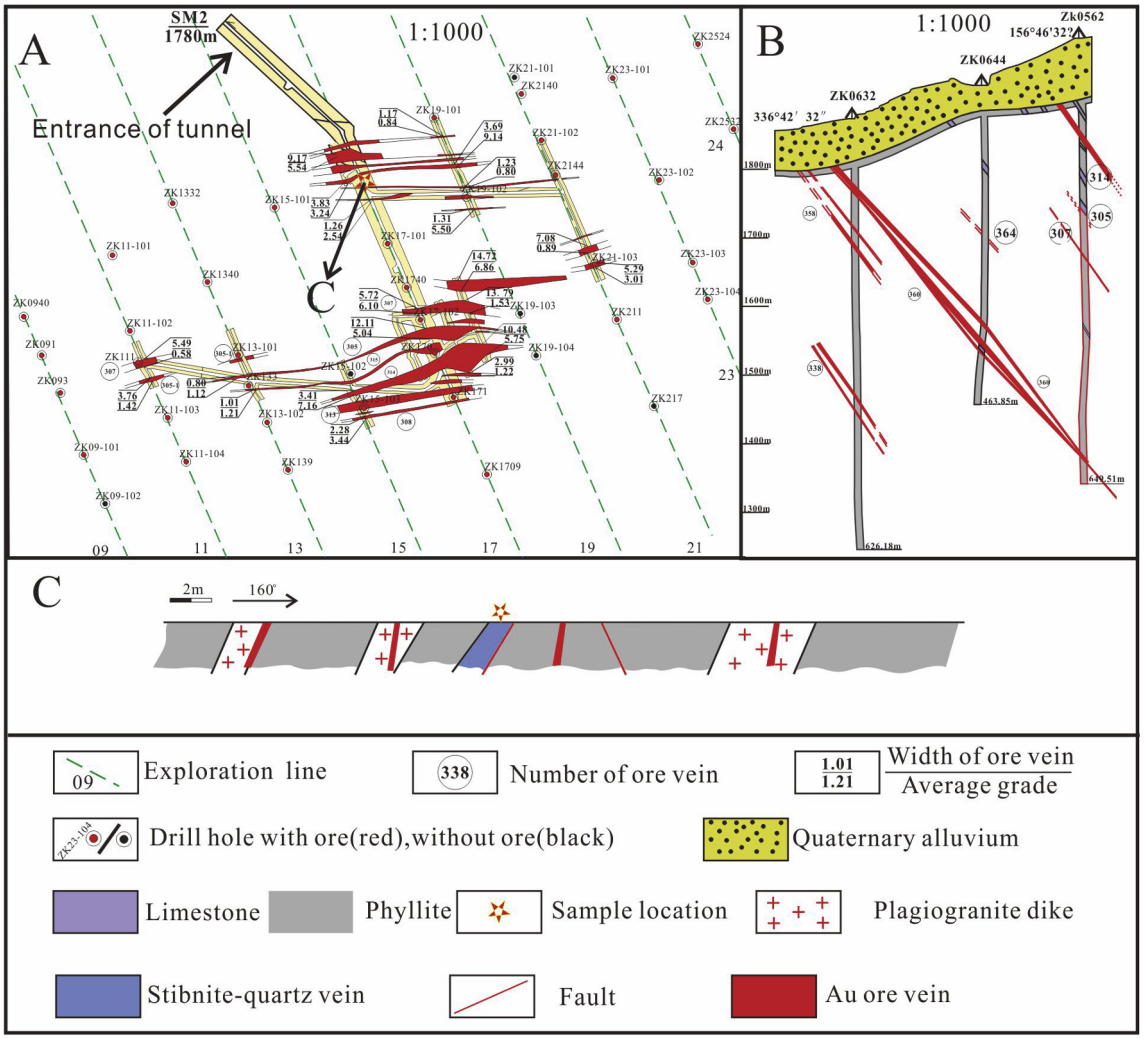

Fig. 3. Horizontal (A) and vertical (B) sections show the shapes of the ore bodies and the sample locations. Au grades gradually pinch out in the vertical section. (C) The profile of the major tunnel SM2 shows the sample locations.

belt. Their cores consist of limestone (Fig. 2). The Anchanghe-Guanyinba fault system and the Getiaowan-Caopingliang anticline, as well as a series of secondary ENE-trending faults jointly control the ore bodies of the Yangshan gold ore belt.

There is no large scale intrusion within or adjacent to the Yangshan ore belt, whereas small intermediate to acidic dikes, ranging from tens of centimeters to several meters in width, are commonly developed within the Middle Devonian metasedimentary sequences (Fig. 2). Among these, the plagiogranite dikes mineralized to form ore bodies especially near the contact with the carbonaceous phyllite. Plagiogranite dikes display porphyritic texture, and are moderate to coarse-grained with plagioclase phenocrysts (45 vol%), in a quartz (30 vol%), potassic feldspar and biotite (10 vol%) matrix, with minor amounts of hornblende, magnetite, zircon, apatite, pyrite and arsenopyrite. Zircon U-Pb dating indicated that these dikes were emplaced between the Late Triassic and the Middle Jurassic (218–179 Ma) (Sun et al., 2012; Yan and Li, 2008; Yang et al., 2015a).

2.3. Mineralization of the Yangshan gold deposits

Four types of gold ore have been recognized in the Yangshan ore belt. The first occurs as stratiform ore bodies in the SHKF3. It consists of bedded carbonaceous or calcareous phyllites intercalated with thick-bedded or lens-shaped limestone, which have undergone greenschist facies metamorphism and strong structural deformation (Fig. 4A–C). Ore minerals include fine-grained (several tens to hundreds of microns in size) pyrite and arsenopyrite, minor galena, chalcopyrite, and sphalerite. Gangue minerals include quartz, sericite, calcite, and clay minerals (e.g. kaolinite, montmorillonite). This type of mineralization occurs mainly in the south of the E-W trending normal fault from Zhangjiashan to the Anba deposit (Fig. 2). The second type of mineralization consists of coarse-grained (0.5 to several centimeters in size) pyrite-quartz veins in black carbonaceous phyllites containing significant organic matter up to 6.6 wt% (Qin and Zhou, 2009) (Fig. 4D). It was discovered in the PD051 Tunnel in the north of the inferred normal fault (the red dotted line in Fig. 2). The ore mineral is the coarse-grained pyrite. The third ore type is the mineralized plagiogranite dike (Fig. 4B, C). The ore minerals are pyrite and arsenopyrite approximately 0.1–1 mm in size. No visible gold was identified in the above three types of ores, pyrite and arsenopyrite are the main Au-carrying minerals. Detailed composition and textural characteristics of the Au-carrying pyrite and arsenopyrite are available in Liang et al. (2013, 2014) and Li et al. (2014). The fourth ore type is a stibnite-quartz vein, which consists of pure quartz aggregates, variably sized needle-shaped

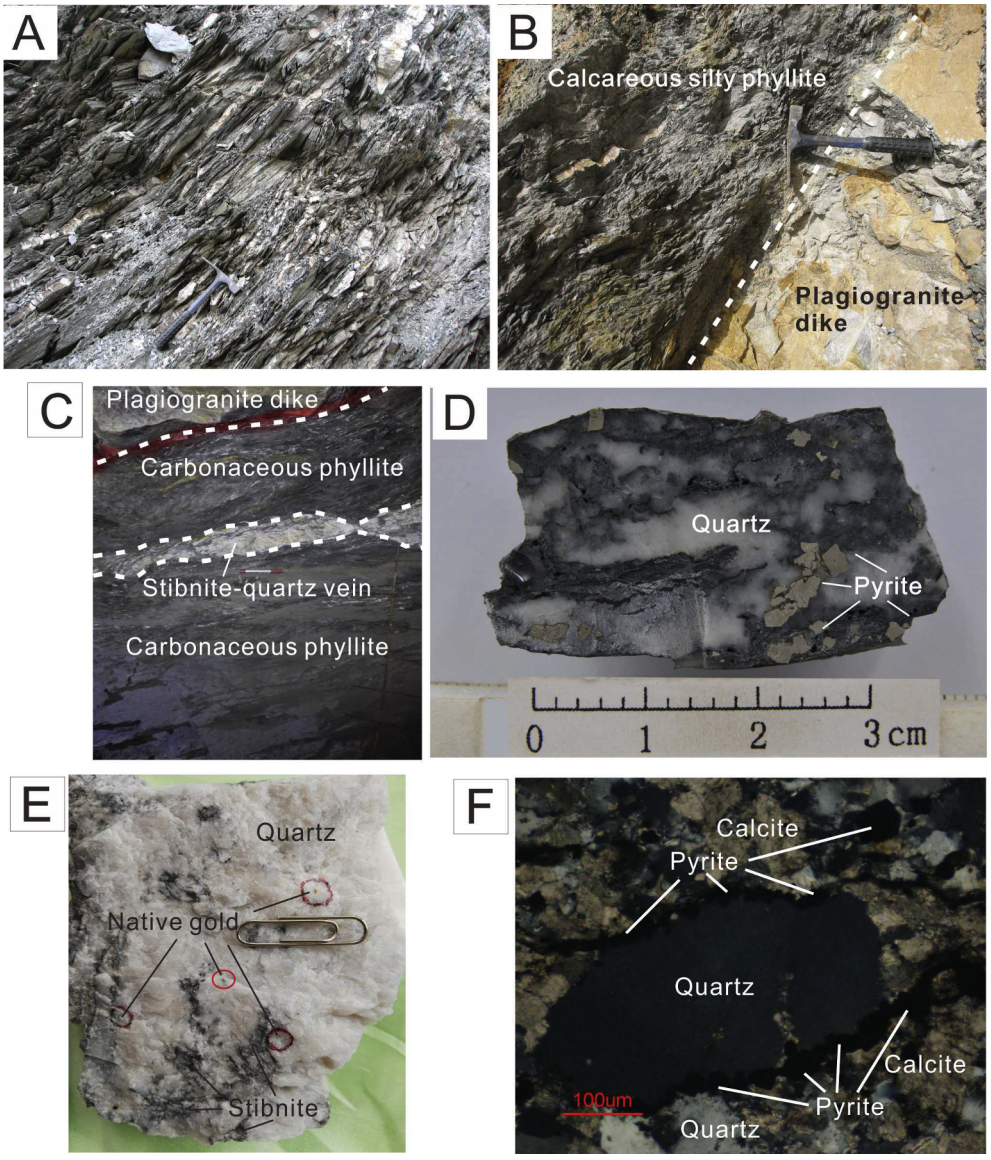

Fig. 4. Photographs of outcrops, hand specimens, and micrographs of ores from the Yangshan gold deposits. A- Carbonaceous phyllite with significant organic matters and bedding parallel quartz veinlets host disseminated fine-grained pyrite and arsenopyrite. B- Calcareous silty phyllite intruded by the plagiogranite dikes ranging from several tens of centimeters to several meters in width commonly have enhanced Au grades on their boundaries. C- Tunnel section shows the major ore-hosting phyllite crossly cut by the plagiogranite dikes and stibnite-quartz veins with a width from several centimeters to several meters. D- Black shales interlayed with the highly deformed bedding parallel quartz veinlets containing coarse-grained pyrites. E- Hand specimen of the stibnite-quartz vein host visible native gold approximately one millimeter in diameter. F- The micrograph of the mineralized limestone shows the alterations of decarbonation, silicification, and sulfidization, which display as the solution of calcite crystals and filling of the newly formed quartz and pyrite.

or anhedral stibnite from 10 to 50 vol%, and minor fine-grained pyrite. Most stibnite-quartz veins are several tens of centimeters in width, and occur along fractures crosscutting phyllite or the contact between the plagiogranite dikes and phyllite (Fig. 4C). Some stibnite-quartz veins cut across the plagiogranite dikes, indicating that the stibnite-quartz vein is late mineralization. Compared with the former three ore types which do not contain visible gold, the stibnite-quartz veins have visible native gold grains varying in diameter from 0.1 to several millimeters (Fig. 4E). The stibnite-quartz veins have the highest Au grades among the four ore types from several tens to hundreds of ppm (our unpublished data). Of the four ore types, the first one contains the largest Au reserve.

Wall rock alteration observed at the Yangshan gold ore belt includes decarbonation, silicification, and sulfidization. Decarbonation is characterized by development of solution fissures in the limestones and silicon-filling. Silicification during the hydrothermal stage (i.e. the main ore stage) occurs as fine-grained or aphanitic quartz filling in the small fractures in the carbonaceous limestone and phyllite. Sulfidation is commonly accompanied by the decarbonation and silicification, and occurs as newly formed fine-grained pyrite grains distributed along the edge of quartz grains or as overgrowths on preexisting synsedimentary pyrites (Fig. 4F).

2.4. Texture and paragenetic sequence of sulfides

2.4.1. Arsenian pyrite

Pyrite is one of the common Au-carrying sulfides. Petrographic observations and EPMA analysis show that the framboidal pyrites in the phyllite and limestone are synsedimentary (pre-ore), and are not associated with the Au mineralization (Fig. 5A). The disseminated pyrites both in the clastic-carbonate sequences and the granitic dikes display two to three zones including an Au, As-poor core; Au, As-rich mantle; and Au, As-poor rim, which corresponds to syngenetic/diagenetic stage, ore-forming event, and post-ore hydrothermal activities respectively (Fig. 5B–D). The coarse-grained pyrites in the pyrite-quartz veins of black phyllites are generally without a zoned texture and host comparative gold with the fine-grained pyrites (Liang et al., 2014). This implies that the coarse-grained pyrites may occur during the main ore stage (Fig. 6).

2.4.2. Arsenopyrite

Arsenopyrite is another common Au-carrying sulfide, which contains an order of magnitude higher gold than pyrite (Liang et al., 2014). Disseminated arsenopyrite occurs both in the clastic-carbonate sequences and the granitic dikes, and displays the same textures as pyrite (Fig. 5D). Considering the texture of the two sulfides, pyrite occurred slightly earlier than arsenopyrite which usually occurs in the main ore stage and is overgrown during the post-ore stage (Fig. 5D).

2.4.3. Stibnite

Coarse stibnite occurs in the stibnite-quartz veins crosscutting both the disseminated clastic rock ore veins and the granitic dikes. It belongs to the last ore stage or post-ore stage (Fig. 4C, Fig. 6).

2.4.4. Gold

Invisible gold is dominant in the Yangshan gold field, and hosted both in the clastic-carbonate rocks and the granitic dikes, in both of which gold exists commonly in solid solution and/or in nano-particles (Liang et al., 2013, 2014). Native gold grains up to millimeter size are only identified in the stibnite-quartz veins of the late ore stage (Fig. 4E, Fig. 6).

2.4.5. Other sulfides

Realgar and orpiment occur occasionally during the post-ore stage in Yangshan. Additionally, very minor chalcopyrite, galena, sphalerite, boulangerite, jamesonite, famatinite, tennantite, and bournonite mostly

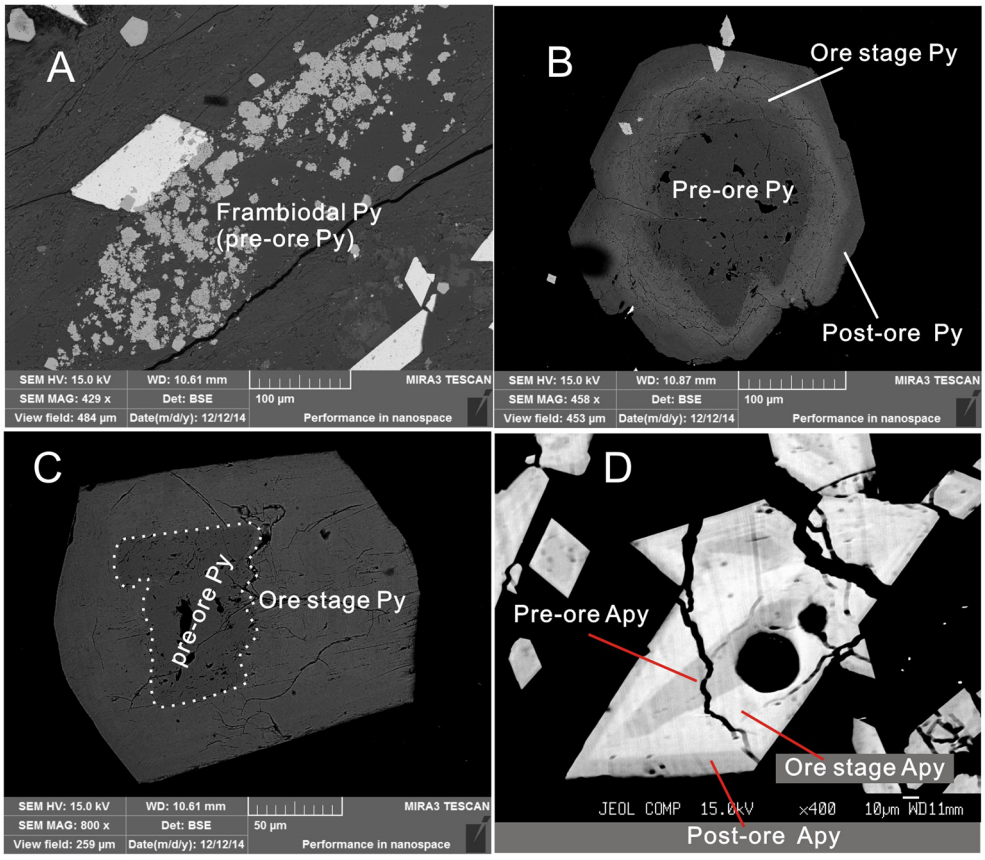

Fig. 5. Backscattered electron (BSE) images show the texture of pyrite and arsenopyrite. A- Framboidal pyrite with very low or without Au and As is pre-ore pyrite (Py). B- Pyrite from the plagiogranite dike of the Anba ore deposit. The core with very low As and Au is identified as pre-ore pyrite, the middle overgrowth with high As and Au, identified as ore stage pyrite, and the outermost rim with very low As and Au, identified as post-ore pyrite. C- Pyrite from the carbonaceous phyllite of Anba ore deposit. The core with very low As and Au is identified as pre-ore pyrite, and the overgrowth rim with high Au and As, identified as ore stage pyrite. D- Arsenopyrite (Apy) from carbonaceous phyllite of the Anba ore deposit, with the similar texture to the pyrite in B.

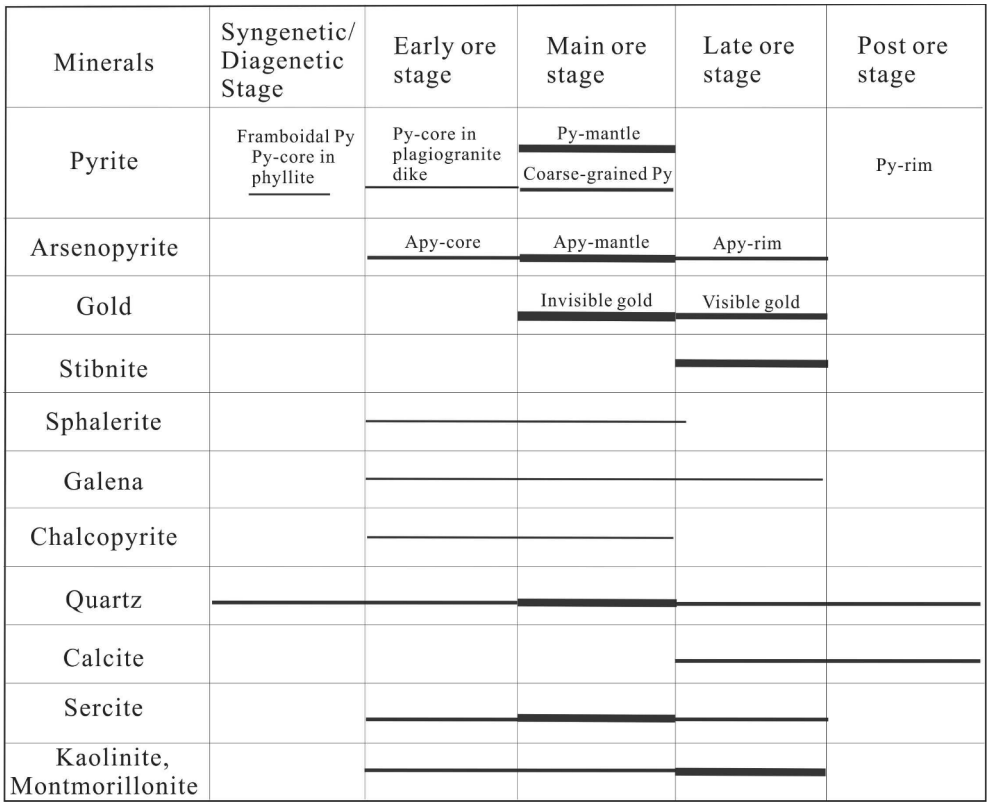

Fig. 6. Paragenetic sequence of the Yangshan gold deposits based on the petrographic observation and EPMA analysis. The bold lines indicate high abundance, the thin lines represent the minor amounts, and the dashed lines indicate uncertainty. Py- pyrite; Apy- arsenopyrite; Core, mantle, rim- the inner, middle, and outer zones of the zoned fine-grained pyrite or arsenopyrite both in the clastic-carbonate formation and the granitic dikes.

occurs as inclusions in pyrite (Li et al., 2014).

The paragenetic sequence of the ore minerals and gangue minerals is summarized in Fig. 6. Preexisting sulfides were overgrown accompanying silicification and sulfidation during the ore stage. Sercite, kaolinite, and montmorillonite formed during the ore stage.

3. Sample preparation and analytical methods

3.1. Sample preparation

Five representative coarse-grained pyrite-quartz vein samples in the black carbonaceous phyllites were collected from the PD051 Tunnel in the Anba deposit (Fig. 2). These samples were double-side polished as thin sections with 0.2–0.5 mm thickness, used for microthermometric analysis and vapor phase component measurement of fluid inclusions. Separates of pyrite and quartz were handpicked from the pyrite-quartz veins under binocular microscope for analysis of noble gas isotopes. Two phyllite ore samples from the zk024 drillhole and four plagiogranite dike samples from the surface outcrops in the Anba deposit were collected (Fig. 2). These samples were mounted and polished as thin sections with thickness less than 0.1 mm, and used for electron probe microanalysis (EMPA). The backscattered electron (BSE) images of pyrite were prepared beforehand for in situ sulfur isotopes determination using NanoSIMS. Before the NanoSIMS analyses, the rectangular thin sections were cut into 25 mm diameter round sections to fit the sample holder. The stibnite-quartz vein sample with visible gold (Fig. 4E) was collected from the 1780 m middle section of the SM2 main tunnel in the Anba deposit (Fig. 3A, C).

3.2. Microthermometric measurements

Fluid inclusions in quartz from the coarse-grained pyrite-quartz veins were examined using a Linkam THMSG 600 programmable heating-freezing stage mounted on an Olympus microscope, calibrated with melting-point standards of pure CO_2 (−56.6 °C) in synthetic fluid inclusions. The uncertainty of temperature measurements in this study was approximately ± 0.2 °C below 50 °C and ± 2 °C above 100 °C. A heating rate of 0.1 °C/min was adopted near the melting temperatures of the carbonic phase, clathrate, and ice. Vapor compositions of fluid inclusions were identified using laser Raman spectroscopy. The salinities of two and three-phase H_2O-CO_2-NaCl inclusions were calculated from the final melting temperature of ice or clathrate following the method proposed by Bodnar (1993) and Collins (1979). The microthermometric measurements were conducted in the Microthermometry Laboratory at the Sun Yat-Sen University.

3.3. Noble gas isotope measurements

Mineral separates of fresh pyrite and quartz were used for noble gas isotopic measurement. Noble gas compositions of fluid inclusions hosted in these minerals were released by stepwise heating, which is a powerful and widely adopted technique in noble gas analysis (Bruno et al., 1997). Pyrite appears to be one of the best preservers for noble gases (Ballentine, 2002; Zhu and Peng, 2015). The cosmogenic nuclides can be ignored because the samples were collected from the underground tunnel (Tunnel PD051). The concentrations and isotopic compositions of noble gases were measured using a MM5400 mass spectrometer in the Key Laboratory of Petroleum Resources Research (Lanzhou), Institute of Geology and Geophysics, CAS. The air standard (AIRLZ2007) is the air sample from Gaolanshan Hill in Lanzhou City ($^4He/^{20}Ne$ = 0.3185, $^4He/^{40}Ar$ = 0.00056328, Ra = $^3He/^4He$ = 1.400E-6, $^{20}Ne/^{22}Ne$ = 9.800, $^{21}Ne/^{22}Ne$ = 0.0290, $^{38}Ar/^{36}Ar$ = 0.1880, $^{40}Ar/^{36}Ar$ = 295.5). The instrumental blank values at 1600 °C: $^4He = 2.46 \times 10^{-10}$, $^{20}Ne = 4.08 \times 10^{-10}$, $^{40}Ar = 1.39 \times 10^{-8}$, $^{84}Kr = 3.07 \times 10^{-12}$, and $^{132}Xe = 1.26 \times 10^{-13}$ respectively (Ding et al., 2014). The results were calibrated by the local air standard and instrumental blank (Ye et al., 2001; Ding et al., 2014). The analytical precision for the noble gas isotopic measurements is better than 10%. The analytical procedures were followed the detailed descriptions by Ye et al. (2001).

3.4. Scanning electron microscopy

Scanning electron microscopy (SEM) backscattered electron (BSE) observations and identification of multiple generations of pyrite are the necessary preparations for in situ sulfur isotopic measurements. SEM observations were performed using a TESCAN MIRA 3 LMH FE-SEM in the Electron Microbeam Analysis Laboratory in University of Science and Technology. A reduced beam current of 5nA was used to improve the resolution and contrast of BSE image of pyrite.

3.5. Elemental mapping and in situ sulfur isotope determination using NanoSIMS

Trace elements mapping and in situ sulfur isotopes of pyrite were carried out using a CAMECA NanoSIMS 50L mass spectrometer at the Institute of Geology and Geophysics, CAS. First, the images of S (^{34}S), As (^{75}As), Se (^{80}Se), Cu ($^{63}Cu^{32}S$), and Au (^{197}Au) of pyrite were acquired by rastering areas using a Cs^+ beam. As a preparation, each $50 \times 50\,\mu m^2$ interest area was pre-sputtered with a primary beam of 1nA for 2 min to remove the carbon coating on the pyrite, and implant enough Cs^+ ($> 10^{17}$ ions per cm^2) into the sample surface to stabilize the yield of the secondary ions. An area ranging from 20×20 to $40 \times 40\,\mu m^2$ was then mapped using a low beam current of 7–10 pA with a diameter of 250 nm. The data was accumulated as images with a pixel resolution of 256×256 for the secondary ions including ^{34}S, ^{75}As, ^{80}Se, $^{63}Cu^{32}S$, and ^{197}Au. Each image contains 3 frames, and was collected over a total analysis time of ~30 min. Individual frames were added together after correction for position shift, using the WinImage software (CAMECA). Then, according to the acquired elemental images, several $2 \times 2\,\mu m^2$ interest areas were selected, and the sulfur isotopic ratio ($^{34}S/^{32}S$) analyses were performed (5–8 min for each area). The sulfur isotopic ratios were corrected for dead-time with instrumental mass fractionation. Balmat pyrite was used as a standard reference, its ratio of $^{34}S/^{32}S$ was confirmed by Ushikubo et al. (2014) with a stable mass spectrometer ($\delta^{34}S_{VCDT} = 16.04 \pm 0.2\%$). The rastering area was $30 \times 30\,\mu m^2$ for the sulfur isotope measurement. Each $30 \times 30\,\mu m^2$ area was given a mean isotopic value from 3 to 6 repeated measurements, with each point area $2 \times 2\,\mu m^2$. The external reproducibility (1SD) of sulfur isotopes is better than 0.5%, and the analytical accuracy is better than 0.6%. To improve the analytical accuracy, $^{32}S^-$ was counted with Faraday cups and $^{34}S^-$ with electron multipliers using a Cs^+ beam current (7 pA, 250 nm in diameter). Detailed instrumental conditions and analytical procedures are available in Zhang et al. (2014, 2017).

4. Results

4.1. Fluid inclusions

Based on petrographic observation of primary fluid inclusions in the ores from the Anba gold deposit, three types of fluid inclusions in quartz formed during the main ore-forming stage have been identified: (1) Single-phase liquid CO_2 inclusions, look dark (Fig. 7); (2) Two-liquid-phase inclusions contain aqueous solution and liquid CO_2 phase varying from 20 to 90 vol% (Fig. 7). This kind of fluid inclusion homogenized to liquid during microthermometry; (3) Three-phase inclusions contain a round vapour bubble of CO_2, a liquid CO_2 phase of irregular in shape, and aqueous solution, with vapor + liquid CO_2 phases less than 50 vol % (Fig. 7). The three phases are visible at room temperatures, and homogenized to liquid upon heating. Among the three types of fluid inclusions, the latter two types are dominant. The third and some of the second types have less than 50 vol% liquid CO_2, and their phase transitions are easy to be observed during microthermometry. Such inclusions were selected for measurement. Co-existence of the three types of fluid inclusions in the Yangshan gold deposit indicates that the heterogeneous fluid, i.e. boiling fluid capture may have occurred during ore deposition. Due to the existence of ore fluid boiling, it is unnecessary to make a pressure correction to the measured temperatures (Zhai et al., 2009).

The microthermometric data is listed in Table 1. The ice melting temperatures (T_m is the starting melting temperature of bulk fluid which was in advance frozen to ice) range from −55.3 to −57.5 °C (n = 60), very close to the triple points of pure CO_2 (−56.6 °C). The clathrate melting temperatures ($T_{m\text{-}clath}$) range from 6.1 °C to 9.0 °C (n = 60), corresponding to salinities of 2.0–7.2 wt% NaCl equiv (Fig. 8A). Two or triple phase inclusions homogenized to the liquid phase (while vapor CO_2 disappeared) at the temperatures ($T_{m\text{-}CO2}$) between 8.3 and 28 °C (n = 60). The final homogenization temperatures ($T_{h\text{-}total}$, the homogenization temperatures of bulk H_2O-CO_2 system) are from 221 to 303.5 °C (Fig. 8B). The melting temperatures in this study are close but slightly higher than the results of Li et al. (2007a) (−61.9 to −56.7 °C) from the Yangshan gold deposit, whereas the bulk homogenization temperatures in this study are similar to their ore stage temperatures (205–284 °C) (Table 1 and Fig. 8B). The estimated lithostatic pressure range from 159 to 354 MPa, corresponding to the ore-formation depth of 6–13 km, similar to the results of Li et al. (2007a) (Table 1).

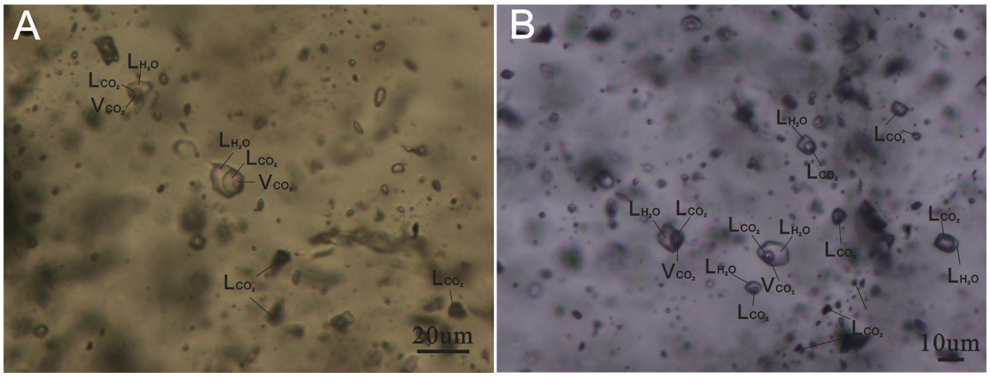

Fig. 7. Fluid inclusions in quartz veins from the Anba ores. A-single-phase aqueous solution and triple-phase fluid inclusions of vapor phase CO_2, liquid CO_2, and aqueous solution; B-single-phase aqueous solution or liquid CO_2, two-phase aqueous solution and CO_2 fluid inclusions, and triple-phase fluid inclusions.

Table 1
Microthermometric data of fluid inclusions of ore-bearing pyrite-quartz veins from the Anba gold deposit.

Sample	n	T_m (°C)	$T_{m\text{-}clath}$ (°C)	$T_{h\text{-}CO2}$ (°C)	T_h (°C)	S (wt.% NaCl)	P (MPa)	H (km)
09PD051-1	12	−57.1 to −56.7	7.2–8.1	20–25	234–303.5	3.7–5.3	190–305	7–11
09PD051-5	37	−57.5 to −55.3	6.1–9.0	8.3–28	221–310	2.0–7.2	159–354	6–13
09PD051-7	11	−57.2 to −56.8	7.9–8.7	14.8–23.0	265–290	2.6–4.1	239 to −285	9–11
†pre-ore stage (C)	53	−60.6 to −56.7	9.8–15	17.8–29.9	255–326 240–320	–	178–222 128–138	
†ore-stage (C + PC)	35	−61.9 to −56.7	10.2–11.6	8.6–29.8	234–284 205–260 179–226	1.4–5	108–115 85–120 162–168	3.3–8.5
†post-ore stage (W)	24	–	–	–	160–210	1.5–2.7	143–148 112	

Note: n-number of data points; Tm- ice point temperature after the bulk fluids were frozen to ice; $T_{m\text{-}clath}$- melting temperatures of clathrate (ice); $Th\text{-}_{CO2}$- homogenization temperatures to CO_2 liquid phases; T_h- total homogenization temperature of H_2O-CO_2 system; S-salinity; P-estimated pressure; H-estimated ore formation depth; C- CO_2-bearing fluid inclusion, PC-pure CO_2 fluid inclusion, W- aqueous fluid inclusion; † data from Li et al. (2007a); – not detected.

4.2. Vapor component of fluid inclusions

A Raman spectroscopic analysis for the vapor phases of fluid inclusions in quartz was performed. The results show that CO_2 is the major volatile component in fluid inclusions, and no N_2, CH_4 or other gases was detected (Fig. 9). This result is consistent with the ice melting temperatures (T_m) which are close to the triple points of pure CO_2 (−56.6 °C).

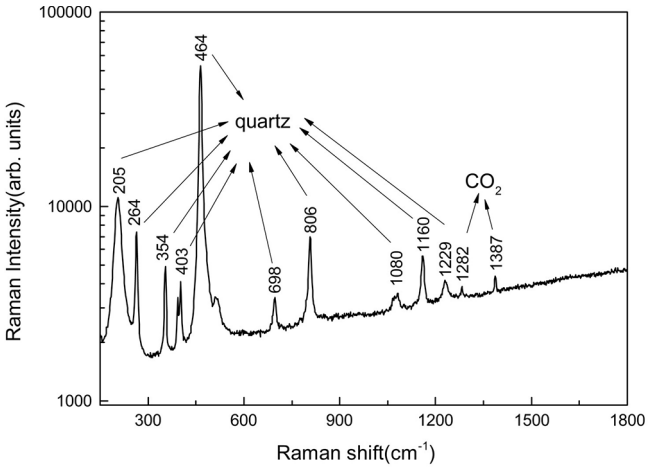

Fig. 9. Representative Raman spectroscopy analysis for the vapor components of the fluid inclusions in quartz of the coarse-grained pyrite-quartz veins from the Anba ore deposit show that the major gas phase is CO_2 without other detectable components such as N_2, CH_4.

4.3. Noble gas isotopes

Six samples including 4 pyrite grains and 2 quartz grains were handpicked from the mineralized coarse-grained pyrite-quartz veins in carbonaceous phyllites representing the main ore stage. Noble gas compositions and isotopic ratios in fluid inclusions were determined. The results are listed in Table 2. The results show that the ^4He and ^3He values are 205–287 × 10^{-7} cm^3STP/g, 13.2–30.7 × 10^{-7} cm^3STP/g in pyrites, and the corresponding values in quartz are 1.61–1.83 × 10^{-7} cm^3STP/g, and 0.136–0.175 × 10^{-7} cm^3STP/g respectively. ^{40}Ar are 14.6–33.8 × 10^{-7} cm^3STP/g, ^{20}Ne from 0.0994 to 0.468 × 10^{-7} cm^3STP/g. The $^3He/^4He$ ratios range from 0.032960 to 0.032960 Ra (Ra is the atmospheric $^3He/^4He$ ratio). The $^{40}Ar/^{36}Ar$ ratios vary from

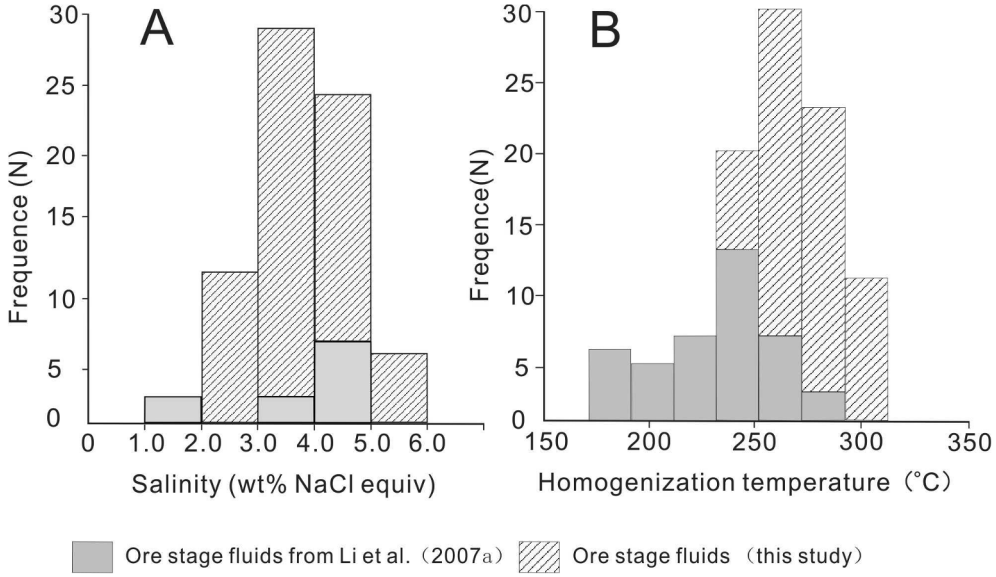

Fig. 8. Salinity and homogenization temperatures of ore fluids during ore stage of the Yangshan gold deposits. Data was compiled from this study and Li et al. (2007a).

Table 2
Noble gas compositions and isotopic ratios of fluid inclusions in pyrite and quartz from the Anba ore deposit.

Sample	Mineral	^{4}He(cm^{3}STP/g)(E − 7)	^{3}He(cm^{3}STP/g)(E − 7)	^{20}Ne(cm^{3}STP/g)(E − 7)	^{40}Ar(cm^{3}STP/g)(E − 7)	^{3}He/^{4}He (*Ra*)	^{40}Ar/^{36}Ar	^{40}Ar*(%)	^{40}Ar*/^{4}He	F^{4}He
09PD051-1	pyrite	215 ± 14	13.605	0.373 ± 0.059	33.8 ± 2.5	0.0452 ± 0.00058	449.8 ± 14.5	34.30	0.0539	17287.9
09PD051-2	pyrite	205 ± 14	21.356	0.468 ± 0.078	14.6 ± 1.1	0.0744 ± 0.00044	434.1 ± 11.2	31.93	0.0227	36829.2
09PD051-3	pyrite	287 ± 19	13.243	0.336 ± 0.034	21.9 ± 1.6	0.0330 ± 0.00010	576.5 ± 4.8	48.74	0.0372	45649.8
09PD051-5	pyrite	271 ± 18	30.693	0.411 ± 0.041	22.4 ± 1.6	0.0809 ± 0.00091	465.7 ± 4.1	36.55	0.0302	34043.1
09PD051-1	quartz	1.83 ± 0.13	0.175	0.123 ± 0.012	22.5 ± 1.6	0.0683 ± 0.0054	601.1 ± 13.2	50.84	0.2508	295.4
09PD051-5	quartz	1.61 ± 0.12	0.136	0.099 ± 0.009	15.6 ± 1.1	0.0605 ± 0.0041	863.0 ± 29.9	65.76	0.3717	538.2

Notes: Ra- the atmospheric ^{3}He/^{4}He ratio(1.384E-6); $^{40}Ar^* = (^{40}Ar)_{sample} \times [1-(^{40}Ar/^{36}Ar)_{air}/(^{40}Ar/^{36}Ar)_{sample}]$; $^{40}Ar^*(\%) = [(^{40}Ar/^{36}Ar)_{sample}-(^{40}Ar/^{36}Ar)_{air}]/(^{40}Ar/^{36}Ar)_{sample}$; $F^4He = (^4He/^{36}Ar)_{sample}/(^4He/^{36}Ar)_{air}$, where $(^4He/^{36}Ar)_{air} = 0.1655$ (Kendrick et al., 2001), F^{4}He values reflect enrichment of ^{4}He in the ore fluids to air; The ratios of ^{38}Ar/^{36}Ar of all samples are below the detection; The error is 1 σ.

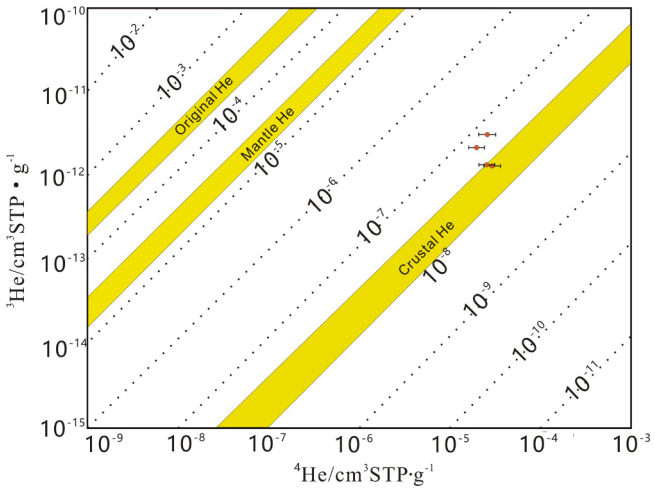

Fig. 10. ^{3}He-^{4}He diagram shows the four pyrite samples from the ore-bearing carbonaceous phyllite of the Anba deposit plot within the crustal He regime. This indicates that no mantle He was involved in the ore formation.

434.1 to 863.0, and the ^{38}Ar/^{36}Ar ratios of the 6 samples are below the detection limit.

The crust typically has ^{3}He/^{4}He ratios of 0.01–0.05 Ra (Tolstikhin, 1978), which are much lower than the ^{3}He/^{4}He ratios of 5–6 Ra from the subcontinental lithospheric mantle (Dunai and Baur, 1995), and much lower than the ^{3}He/^{4}He ratios of mantle (R/Ra ≈ 8 or higher) (Graham, 2002).

The F^{4}He values (the ^{4}He/^{36}Ar ratios of samples relative to the atmospheric ^{4}He/^{36}Ar ratio of 0.1655, from which the atmospheric He contribution to ore fluids can be estimated) of the 6 samples range from 295.4 to 45650, much higher than 1, indicating that the contributions of atmospheric He to the ore fluids in the Yangshan gold deposits are negligible.

The ^{3}He-^{4}He isotopic evolutionary plot shows that the He isotopic compositions of the ore fluids in the 4 pyrite samples fall into the scope of the crust-derived He (Fig. 10). In addition, the 6 samples of pyrite

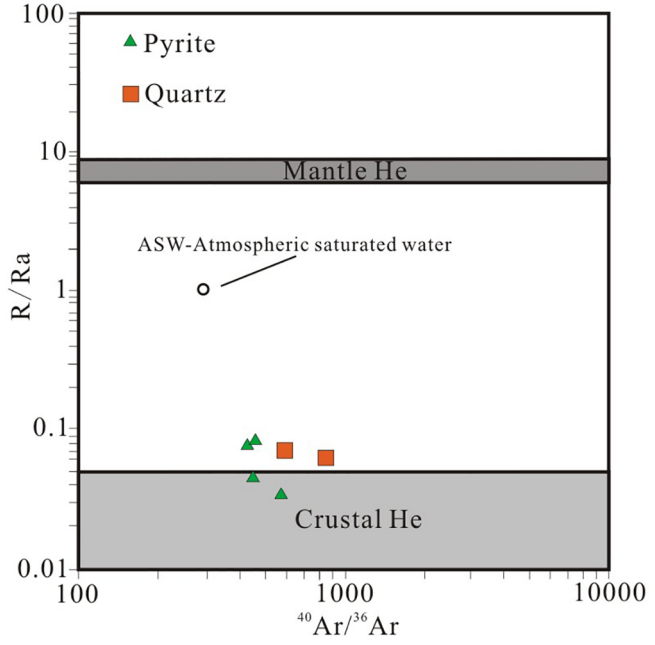

Fig. 11. R/Ra-^{40}Ar/^{36}Ar diagram shows the two quartz and four pyrite samples from the Anba deposit plotting nearby crustal He area. This implies that little mantle component is involved in the ore formation.

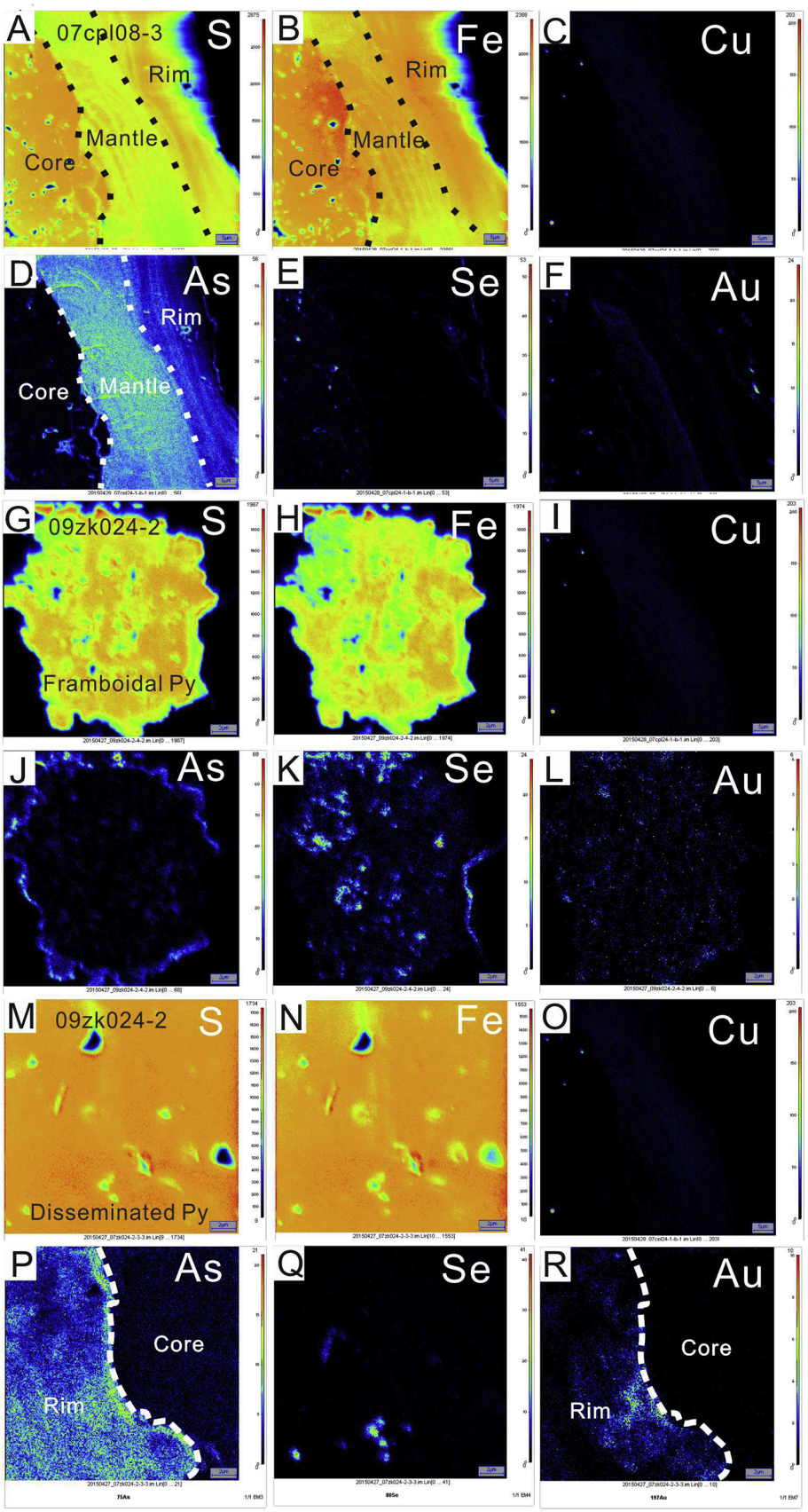

Fig. 12. Nano-SIMS multiple element maps of pyrites from the Yangshan gold deposits. A to F- Trace elemental maps of the pyrites from the mineralized plagiogranite dikes. Three-zoned overgrowth zones are shown in the ^{75}As maps, and Au is hosted in the middle zone (mantle). G to L- Elemental maps of the framboidal pyrite from the carbonaceous phyllite show lower Au, Cu and higher As, Se. M to R- Elemental maps of the pyrite from the mineralized carbonaceous phyllite show As and Au hosted in the overgrowth rim.

and quartz also fall into the crust-derived source in the diagram of R/Ra vs $^{40}Ar/^{36}Ar$ (Fig. 11).

4.4. NanoSIMS elemental maps of pyrite

We obtained NanoSIMS multiple element maps including major elements of S, Fe, and the minor or trace elements As, Cu, Se, and Au of the three types of pyrites from the mineralized granitic dike (the sample 07cpl08-3, Fig. 12A–F), framboidal pyrite (the sample 09zk024-2, Fig. 12G–L), and the carbonaceous phyllite ore (the sample 09zk024-2, Fig. 12M–R). The maps show that: a) framboidal pyrite contains very low As and Au, and is not ore-related; b) Au distributions in pyrites from the granitic dikes and phyllites are heterogeneous with high Au in the middle overgrowth zones. No isolated native gold particles from submicron to nano-scale were identified (Fig. 12F, L, R); c) three episodic magmatic-hydrothermal activities (Fig. 12A, B, D) were recorded, and the main ore formation event was marked by the middle As, Au-high zones (Fig. 12 D, F, P, R); d) the ore fluids are characterized by higher As, Au, Se, and relatively lower Cu.

4.5. In situ sulfur isotopes of pyrite

Sulfur isotopes of pyrite in the mineralized plagiogranite dikes and carbonaceous phyllites are listed in Table 3. To present the sulfur isotope distribution in different overgrowth generations within individual pyrite grain (i.e. inner cores, mantles and outermost overgrowth rims), the sulfur isotopic values are plotted on the BSE images of the corresponding pyrites (Fig. 13). The results show that the framboidal pyrites have extreme low $\delta^{34}S$ values from −23.8% to −20.9% (Fig. 13A). The pyrites from the plagiogranite dikes have a relatively narrow $\delta^{34}S$ range from −7.3 to 1.0% (Fig. 13B–D) (the value of −7.3% in Fig. 13B deviates from 0, likely derived from contamination by the sedimentary S), whereas those from carbonaceous phyllites have wider $\delta^{34}S$ values ranging from −27.8 to 1.3% (Fig. 13E, F). We can see that different generations of pyrites in the plagiogranite dikes have $\delta^{34}S$ values around 0% with small variation (Fig. 13B–D). In contrast, the sulfur isotopic distribution in the pyrites from the carbonaceous phyllites displays different patterns. The cores have $\delta^{34}S$ values lower than −20%, whereas the rims have higher $\delta^{34}S$ values from −5.1 to 1.3% (Fig. 13E, F). The cores of the pyrite in the carbonaceous phyllites share the similar S isotope features to the framboidal pyrites, both have the low $\delta^{34}S$ values (Fig. 13A, E, F).

Table 3
Sulfur isotopes of pyrites from the Anba deposit of Yangshan gold ore belt.

Sample No.	Lithology	Spot location	$\delta^{34}S$ (%)	1σ (%)
07cpl08-3-1	Plagiogranite dike	rim	−1.6	0.18
		core	1.3	0.15
07cpl08-3-2	Plagiogranite dike	rim	1.0	0.19
		rim	0.8	0.18
		core	−3.4	0.16
		core	−4.4	0.17
		core	−4.4	0.16
		rim	−7.3	0.17
07cpl24-1	Plagiogranite dike	rim	−1.3	0.14
		mantle	−2.6	0.21
		core	0.0	0.14
07cpl24-1-b2	Plagiogranite dike	rim	−3.6	0.16
		mantle	−4.5	0.18
		core	0.4	0.15
09zk024-2-1	Carbonaceous phyllite	rim	−3.3	0.15
		core	−26.3	0.17
		core	−25.4	0.14
		rim	1.3	0.15
09zk024-2-3	Carbonaceous phyllite	rim	−5.1	0.14
		rim	−3.3	0.15
		core	−26.5	0.17
		core	−27.8	0.14
09zk024-2-4	Carbonaceous phyllite	Framboidal pyrite	−23.8	0.14
			−21.9	0.15
			−20.9	0.15

5. Discussion

5.1. The nature and origin of ore fluids of the Yangshan gold deposits

5.1.1. Constraints from the microthermometry and noble gas isotopes

It is well known that low to moderate ore-forming temperature, low salinity, CO_2-rich ore fluids, and hosted by metamorphic rocks (most are at least greenschist facies) are of typical characteristics of orogenic gold deposits (Goldfarb and Groves, 2015; Groves et al., 1998; Kerrich et al., 2000; Mernagh et al., 2007). The Yangshan gold deposits have the formation temperatures from 200 to 300 °C, salinities of 2–7 wt% NaCl equiv, and are hosted in the greenschist facies metamorphic clastic rocks of the SHKF. These features imply that the deposits share the common features with orogenic gold deposits. In fact, there are dozens of sediment-hosted disseminated gold deposits in western Qinling region, which were classified as Carlin-type, Carlin-like, and orogenic type (Chen et al., 2004; Liu et al., 2015a; Mao et al., 2002; Zhang et al., 2003a,b) (Fig. 1). These deposits are commonly hosted in sub-greenschist to greenschist facies metaclastics with minor metavolcanic rocks and limestone interlayers. Available microthermometric dada show that these gold deposits possess the common ore fluids characteristics such as low to medium formation temperatures, low salinities and aqueous CO_2-bearing (or CO_2-rich) fluids with small amounts of CH_4, N_2 except individual deposit (e.g. Shuangwang and Zhaishang deposits) with the salinities > 20 wt% NaCl equiv and containing daughter minerals (Table 4). Someone suggested these gold deposits are the products of Qinling orogenesis, classified them into three types of orogenic, Carlin-type, and Carlin-like. The Yangshan gold deposits belong to the Carlin-like style (Liu et al., 2015a).

Mantle, crust, magma-derived fluids and meteoric water all likely played important roles during gold ore formation, and noble gas isotopes can provide constraints on the origin of ore fluids (Burnard et al., 1999; Graupner et al., 2006; Zhu et al., 2013). Pyrite appears to be one of the best preservers for noble gases due to the extremely low concentration of U, Th and K in sulfides (Ballentine, 2002; Burnard et al., 1999; Zhu et al., 2013; Zhu and Peng, 2015). The F^4He values of pyrite (> 10000) and quartz (> 200) (Table 2) are remarkably higher than that of the atmosphere ($F^4He = 1$, Kendrick et al., 2001). Thus the contributions of atmospheric He to the ore fluids is negligible. Moreover, because in-situ additions of radiogenic ^4He, ^{40}Ar and cosmogenic nuclides are negligible for our sulfide and quartz samples collected from the underground exposures (Tunnel PD051), the measured compositions of noble gas isotopes can truly represent the initial composition of the fluid inclusions. $^3He/^4He$ ratios of the pyrite and quartz are within a low and narrow range of 0.033–0.0809Ra (Table 2). The helium isotopic ratios are consistent with the crust-derived helium isotopic ratios of 0.01–0.05Ra (Tolstikhin, 1978) without mantle-derived fluid involvement.

The measured $^{40}Ar/^{36}Ar$ values of fluid inclusion in the pyrite and quartz range from 434.1 to 863, higher than the ratio of $^{40}Ar/^{36}Ar$ of air-saturated water (295.5). This indicates a significant proportion of $^{40}Ar^*$ (radiogenic ^{40}Ar) either from a mantle origin or the radiogenic decay of ^{40}K in crust. The proportion of radiogenic $^{40}Ar^*$ ($^{40}Ar^*$ %) estimated from the Yangshan samples are 31.93–65.76%, with an average of 44.69%. That is, the corresponding contributions of atmospheric Ar are 34.24–68.07%, with an average of 55.31%. This indicates that a considerable fraction of Ar in the ore fluids of the Yangshan deposits derived from the atmosphere. This means that the air-saturated meteoric water is involved in the mineralization. This

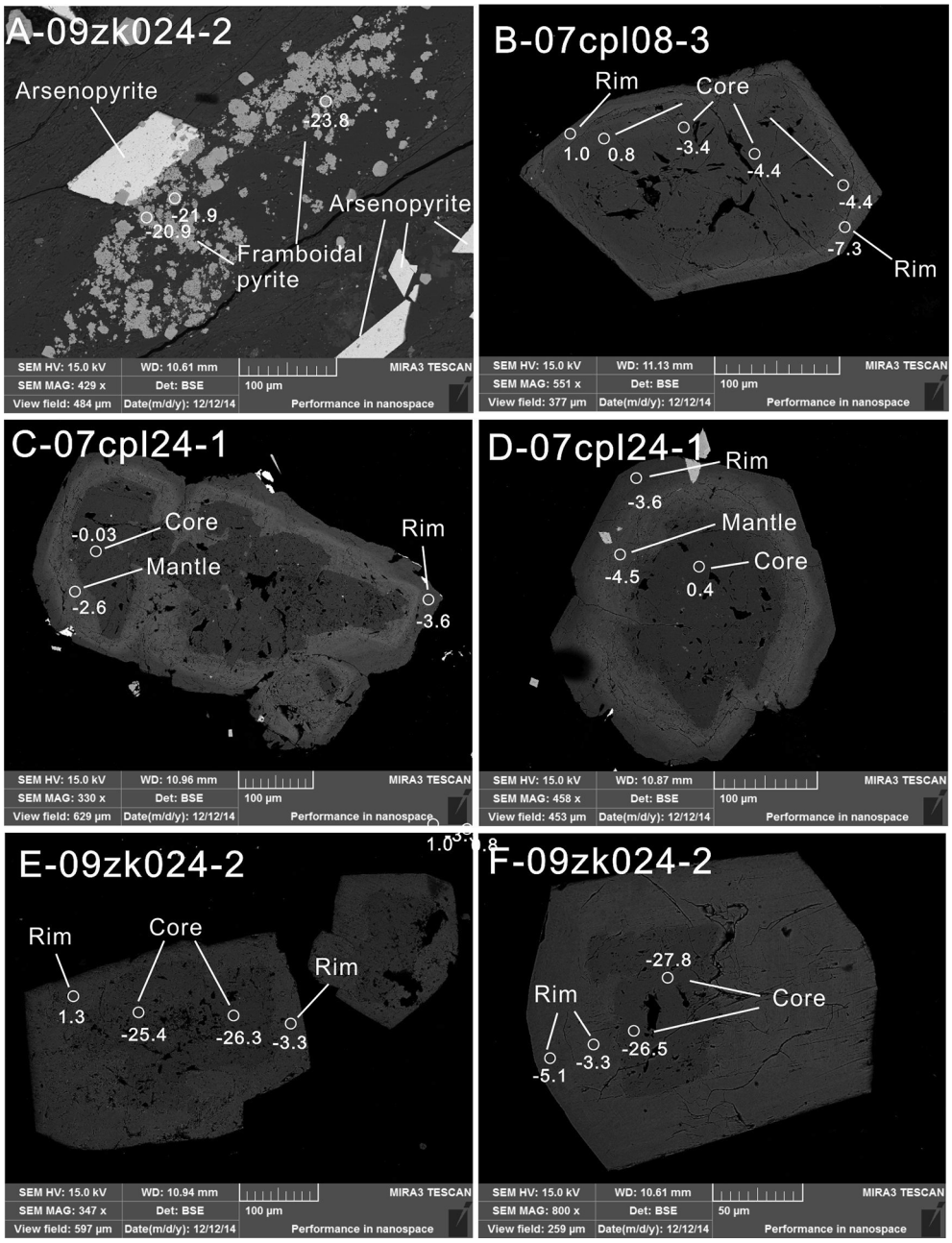

Fig. 13. Sulfur isotope distribution within pyrite from Yangshan. A-Sulfur isotopes of the framboidal pyrite from the phyllite; B to D- Sulfur isotopes of pyrite from the plagiogranite dike show similar isotopic features among different overgrowth zones. This implies that the mineral generations share the identical sulfur source (i.e. magmatic sulfur); E, F- Au-carrying pyrites from the carbonaceous phyllite have two types of sulfur isotopes. The core portions are similar to the framboidal pyrites, and the overgrowth rims are similar to the pyrites from the plagiogranite dikes.

agrees well with the low ratios of $^{3}He/^{4}He$ mentioned above and the extensive exposure of intermediate-acidic dikes in the Yangshan gold ore field. The higher $^{40}Ar/^{36}Ar$ values likely derived from isotopic water-rock exchange between the penetrative meteoric water and the ubiquitous intermediate-felsic intrusive dikes with radiogenetic ^{40}Ar in the Yangshan gold ore field (Ding et al., 2014; Liang et al., 2014).

The $^{40}Ar^{*}/^{4}He$ values (0.0227–0.0539) of the Yangshan pyrite samples (Table 2) are far below the crustal and mantle $^{40}Ar^{*}/^{4}He$ production ratios of 0.2 and 0.5. This indicates that the circulating meteoric waters preferentially acquire more radiogenic He relative to Ar from the water-rock exchange. Since minerals in crustal rocks have higher closure temperatures for Ar than He, He will be lost preferentially at lower temperatures by diffusion (Lippolt and Weigel, 1988). Argon is hosted predominantly in potassium feldspar and mica. Radiogenic $^{40}Ar^{*}$ is retained by feldspar below 200 °C, by biotite below 280 °C, and by muscovite below 350 °C (Mcdougall and Harrison, 1999), whereas He is mobile beyond 200 °C (Stuart et al., 1995). The homogenization temperatures of the Yangshan Au deposit are from 221 °C to 310 °C (Table 1). Under this temperature more He was extracted from the host rocks and entered the ore-forming system than Ar.

5.1.2. Sulfur sources

Previous sulfur isotope analyses of pyrite, arsenopyrite and stibnite from Yangshan yielded $\delta^{34}S$ values of −4.2 to 12.5%, which have been interpreted to have both sedimentary and magmatic origins (Li et al., 2012). Available $\delta^{34}S$ values of sulfides such as pyrite, arsenopyrite,

Table 4
Characteristics of ore fluids of representative sediment-hosted gold deposits in western Qinling orogen and comparison with Carlin-type gold deposits in Nevada.

Deposits	Tonnage (t)	Type	Host rock	Inclusion type	Temperature (°C)	Salinity (wt% NaCl equiv.)	References
Huachanggou	10	Orogenic	Spilite + Phyllite + limestone	Aqueous, CO_2-bearing fluids	240–320	4–10	Liu et al. (2016)
Liziyuan		Orogenic	Greenschist facies Metavolcanic rocks	Aqueous, CO_2-rich fluids	240–280	3–8	Yang et al. (2012)
Shuangwuang	> 80	Carlin-like	Silty phyllite and limestone	Aqueous, CO_2-rich fluids	240–360	2–23	Liu et al., 2011; Liu et al., 2015a
Liba	80	Carlin-like	Slates, siltstone and phyllite	Aqueous, CO_2-bearing fluids	320–400	8–14	Zhang et al. (2004b)
Jinshan	31	Carlin-like	Phyllite + minor limestone	Aqueous, CO_2-rich fluids	280–370	1.5–5 (H_2O-CO_2 fluids); 5–11 (aqueous fluids)	Zhang et al. (2002)
Jinlongshan	> 150	Carlin-type	Carbonaceous slate and siltstone	Aqueous, CO_2-bearing fluids	180–220	5–8	Zhang et al. (2002)
Laerma	> 50	Carlin-type	Siliceous rocks and slates	Aqueous, CO_2-bearing fluids	200–250	5–12	Zhang (1993)
Maanqiao	> 50	Carlin-like	Carbonaceous phyllite + carbonate	Aqueous, CO_2-rich fluids	139–283	< 9	Zhu et al., 2009
Baguamiao	106	Orogenic	Siltstone, silty phyllite + limestone	Aqueous, CO_2-rich fluids	240–300	4–10	Qian et al., 2003; Wei, 2007
zhaishang	127	Carlin-like	siltstone, calcareous slate and argillaceous limestone	Aqueous-solution two-phase inclusions + CO_2-rich three-phase inclusions	105–372	0.7–23.11	Liu et al., 2015b
Jianchaling	52	Carlin-type	Dolomite + minor ultramafic rocks	–	190–310	–	Yue et al. (2013)
Dashui	90.5	Carlin-type	Carbonate	–	105–400	2.96–6.74	Li et al. (2007b);
Yangshan	> 300	Carlin-like	Carbonaceous phyllite + minor plagiogranite dikes	Aqueous, CO_2-rich fluids	200–300	2–7	Li et al. (2007a) and this study
Carlin-type deposits in Nevada, US	Supergiant	Carlin-type	Hydrothermally altered carbonaceous silty carbonates	Aqueous fluids containing CO_2, minor CH_4, sufficient H_2S	180–240	2–3	Cline et al., 2005; Colgan et al., 2014

Note: Au tonnage (t) data of the gold deposits are from Liu et al., 2015a.

marcasite, pyrrhotine, galena, and stibnite from other sediment-hosted gold deposits in western Qinling orogen are highly variable. This was interpreted as multiple sulfur sources of synsedimentary sequences, magmatic fluid or mantle fluid to be involved into ore formation (Liu et al., 2015a, b; Liu et al., 2016). However, all of these studies were carried out on the sulfide separates, which commonly consist of multiple overgrowth generations including synsedimentary or diagenetic (pre-ore), ore stage, and post-ore pyrites (Fig. 5). Thus, bulk mineral separate analysis for sulfur isotopes provided ambiguous information about the source of the ore fluids (Kesler et al., 2003, 2005). Ma et al. (2018) compiling in-situ S isotope data of the representative gold deposits in the south and north subzones of the western Qinling orogen, suggested that the metals and S in the south belt likely came from a deep magma source, whereas those in the north belt may derive from the Devonian graben basins. Our results revealed two distinct types of sulfur sources. The inner cores of zoned pyrites from the carbonaceous phyllites have $\delta^{34}S$ values of −25.4 to −27.8% (Fig. 13E, F) similar to the framboidal pyrites (−20.9 to −23.8%, Fig. 13A). This is a typical sulfur of reduction of seawater sulfate, indicating a synsedimentary origin (Chang et al., 2008, Zhao et al., 2018). Accordingly, these portions/pyrites (i.e. the cores and framboidal pyrites) contain low Au and As (Fig. 5, Fig. 12) (Liang et al., 2014). In contrast, the outermost rims of zoned pyrites in phyllites have a narrow $\delta^{34}S$ range of −5.1 to 1.3% (Fig. 13E, F), similar to that of the pyrites from the mineralized plagiogranite dikes (Fig. 13B-D), which have the three-zoned texture (i.e. core, mantle, and rim), and have similar sulfur isotopes in each zone ($\delta^{34}S$ from −7.3 to 1.3%). Correspondingly, those portions of pyrite have much higher Au and As than the cores and framboidal pyrites (Liang et al., 2014; Zhao et al., 2018). This means that pyrites during the synsedimentary/diagenetic stage did not concentrate enough Au to form ore. Au was likely introduced by a subsequent hydrothermal event, which led to the preexisting pyrite overgrowth. The ore related pyrites in the phyllites have similar S isotopic range with those in the mineralized plagiogranite dikes of the Yangshan gold belt ($\delta^{34}S$ = −7.3 to 1.3%) (Fig. 13B–F). Comparison shows that the ore related pyrites both in phyllites and dikes in the Yangshan gold deposits share similar S isotopic features with the pyrites in the Shuiyindong gold deposit in southwestern China ($\delta^{34}S$ = −2.6 to 1.5%, Hou et al., 2016), and the Carlin-type gold deposits in Nevada ($\delta^{34}S$ = −1 to 4%, Kesler et al., 2005). Sulfur was suggested to derive from either sedimentary or magmatic source in Shuiyindong (Hou et al., 2016), and from a magmatic-hydrothermal fluid in Nevada (Muntean et al., 2011), respectively. Though the viewpoint of a single, ubiquitous ore fluid (e.g. metamorphic fluid) in varying structural settings, rather than from the involvement of oxidised ore fluids (e.g. magmatic fluid) from a different source, was proposed for the formation of the orogenic gold deposits (Hodkiewicz et al., 2009), a distribution pattern of Au (As) vs $\delta^{34}S$ in pyrites should be noticed here (Fig. 14). The pattern of higher Au (As) vs lower $\delta^{34}S$ values in the pyrite, obtained by the in-situ techniques, for example, LA-ICP-MS and EMPA for Au, As concentrations and NanoSIMS for S isotopes, are also revealed in other Carlin-type and orogenic gold deposits such as Shuiyindong and Lannigou gold deposits, in Guizhou, southwestern China, Carlin-type gold deposits in Nevada, the Archean orogenic gold deposits in Western Australia (Fig. 15). This pattern cannot be interpreted by the escape of reduced gas (e.g. H_2S) from the primary Au-carrying fluid triggered by the pressure fluctuation (Hodkiewicz et al., 2009 and references therein). If release of reduced gas caused by the pressure fluctuation have resulted in oxidation of ore fluid, triggering Au precipitation, an opposite pattern of higher Au (As) vs higher $\delta^{34}S$ in the ore stage pyrites would be expected, not the pattern of high Au (As) vs low $\delta^{34}S$ as seen here. Moreover, the pressure fluctuation model would see a continuous rise of $\delta^{34}S$ of the ore fluid, not a random, episodic fluid documented by the zoned pyrites (Figs. 5B–D, 13). Decarbonization, silicification, and sulphidation of wall-rock are the key fluid-rock interactions during ore formation, and need an acidic, Si-enriched fluid with dissolved anion of S^{2-} (H_2S or

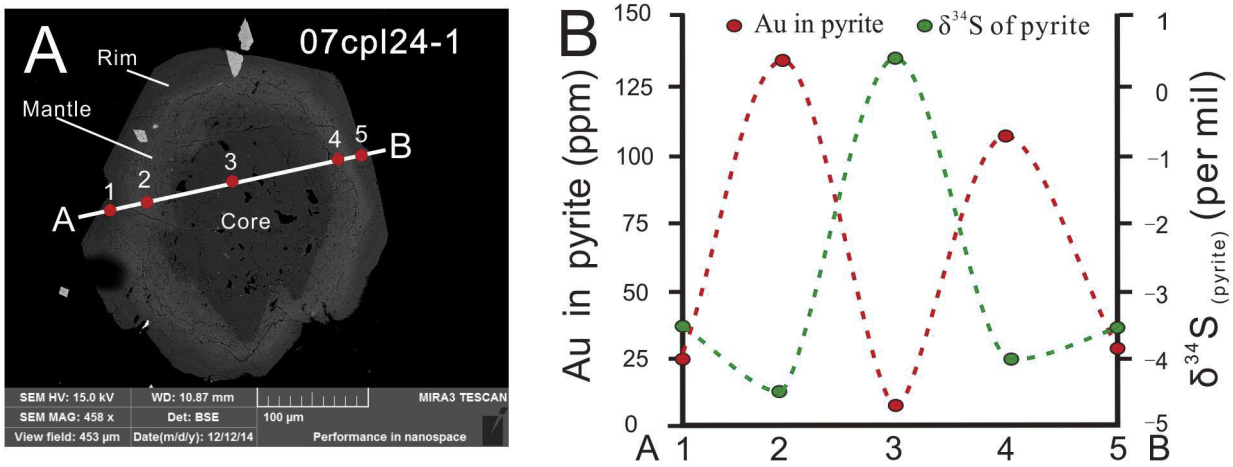

Fig. 14. Profile of Au concentrations vs sulfur isotopic values in pyrite grain from the Anba deposit, Yangshan gold field. A- BSE image of the pyrite shows three growth stages of pre-ore (Core), ore stage (Mantle), and post-ore (Rim). B- Profiles of Au contents (red dash line) and sulfur isotopic values (green dash line) along the line in the map shown in (A). The profiles show the pattern of higher Au vs lower $\delta^{34}S$ values (and vice versa) in the pyrite. Au concentrations in the pyrite are from Liang et al. (2014). (For interpretation of the references to colour in this figure legend, the reader is referred to the web version of this article.)

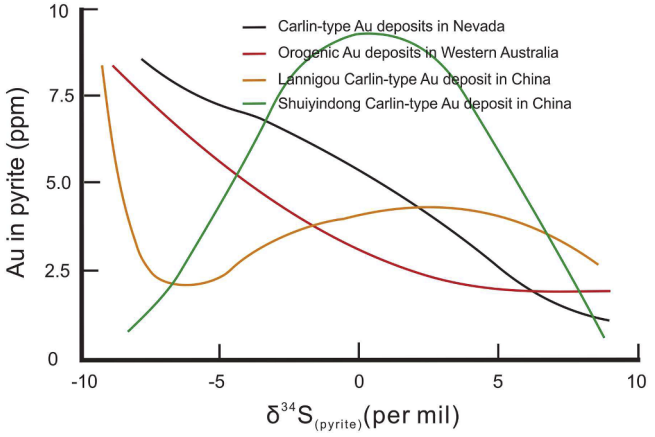

Fig. 15. Plot of Au values in whole-rock (orogenic gold deposits in Western Australia) or pyrites (Carlin-type gold deposits in Nevada, America and in southwestern China) vs in-situ sulfur isotopic values of pyrites from orogenic and Carlin-type Au deposits shows the association of higher Au corresponding to lower sulfur isotopic values. Original data are from Hodkiewicz et al. (2009), Hou et al. (2016), Barker et al. (2009), and Yan et al. (2018).

HS^-) (Cline et al., 2005). Considering the distribution pattern of Au, trace elements and sulfur isotopes in the pyrite, it appears mostly likely that the fluid with S, As, and Au etc. exsolving from a deep magmatic chamber are introduced into the sedimentary rock system leading to overgrowth of the preexisting *syn*-sedimentary pyrites and gold deposition. This interpretation is in agreement with the geological observation that the intermediate-acid intrusive dikes crop out extensively and mineralized themselves in the Yangshan ore field, which are suggested to be closely associated with gold deposition (Lei et al., 2010; Liang et al., 2014; Qi et al., 2005). The larger deviation of the S isotopes from 0% (a magmatic source, Ohmoto, 1972) of the ore related pyrites may derive from the contamination by the sedimentary S source during the magmatic hydrothermal fluid ascending to the surface. Of course, the S isotopic features of the ore related pyrite alone can't rule out the metamorphic fluid to be involved in the mineralization in the Yangshan gold deposits. In order to resolve this question, more systematical determinations of the correlation between Au contents and the corresponding S isotopic values of pyrite both in the host rocks and ore are needed.

5.2. Implications for Au source, depositional mechanism, and genetic style of the Yangshan gold deposits

The carbonaceous sedimentary rock source model highlights that gold mineralization occurred locally within the basin without introduction of Au out of the basin by late hydrothermal/metamorphic fluids (Chang et al., 2008; Large et al., 2009, 2011; Pitcairn et al., 2006). They suggest that pyritic carbonaceous sediments with higher Au concentration (for example more than 250 ppb) have the capability to form economic gold deposits. Whereas the magmatic-hydrothermal model specially proposed for Nevada's Carlin-type gold deposits claims that the gold is derived from deep magma (Kesler et al., 2005; Muntean et al., 2011). One of the evidences of magmatic model are from a strong spatial and temporal association between the Eocence intrusive-volcanic bodies and the gold deposits (Henry and Boden, 1998; Ressel et al., 2000; Ressel and Henry, 2006). In addition, the narrow distribution near 0% of sulfur isotopes of Au-carrying pyrites from Nevada's gold deposits provided support for the magmatic-hydrothermal model (Barker et al., 2009; Kesler et al., 2003, 2005). For the Yangshan gold deposits, we can see the following macro- and micro-scale characteristics: (1) Intermediated-acid intrusive dikes commonly distribute along the ore-controlling Anchanghe-Guanyinba fault zone (Fig. 2). Of these, the plagiogranite dikes mineralized themselves are assumed to be coeval with the dominant gold mineralization of the carbonaceous phyllite (Ding et al., 2014; Li et al., 2014; Liang et al., 2013, 2014); (2) The Au, As-rich overgrowth zones of the pyrites in the carbonaceous phyllite have similar $\delta^{34}S$ values to the pyrites from the mineralized plagiogranite dikes (which has a bias of −7.3% in Fig. 13B, likely derived from the contamination of sedimentary S). The similar Au-As-$\delta^{34}S$ patterns of pyrites in the phyllite and dikes in Yangshan imply that the gold mineralization should have a single ore fluid source. (3) Ore related overgrowth zones of pyrites of Yangshan have similar Au-As-S isotope pattern to the Nevada's Carlin-type gold deposits (Barker et al., 2009). (4) Very low Au concentrations in synsedimentary pyrites (Liang et al., 2014; Li et al., 2014; Zhao et al., 2018) imply that the sedimentary rocks are not capable of being ore sources. And ore formation needs an exotic introduction of Au. For example, a deep magma chamber can partition Au as a bisulfide-complex to an aqueous vapor to form ore fluids (Heinrich, 2005). (5) The distribution of invisible gold (Fig. 12F, R) implies that the overgrowth of preexisting pyrite by the Au-rich fluid is the Au precipitation progress. It is thus not necessary to invoke the oxidation of the ore fluids caused by pressure fluctuation or phase separation (Hodkiewicz et al., 2009). After all, the Au and S are

transported together in the ore fluid, and added into the host rock during the ore-forming process (Chang et al., 2008).

Various models in terms of the sediment-hosted disseminated gold deposits in western Qinling region have been debated for decades, and many viewpoints have been proposed (Chen et al., 2004; Zhang et al., 2003). Since the discovery of the Yangshan gold deposits, diverse genetic models have been proposed such as Carlin-type (Chen et al., 2004; Liang et al., 2013), Carlin-like (Liu et al., 2015a), epizonal orogenic type (Li et al., 2014), epithermal style (Li et al., 2010), and even Yangshan-type (Li et al., 2007a). In fact, some scholars suggested that the Yangshan gold deposit share the characteristics both Carlin-type and orogenic gold deposits (Li et al., 2007a; Liang et al., 2014; Liu et al., 2015a; Mao et al., 2002). The vital issue in terms of the genesis model of the Yangshan gold deposits lie in identification the sources of ore fluids (e.g. S^{2-} or HS^{-}) and metals (e.g. Au, As, Hg, Sb, Tl etc.). The data set presented in this study provides information on the nature and origin of ore fluids and metals suggest a possible deep magmatic-hydrothermal origin as discussed above. Another key factor that strongly constrains the origin and genetic style is ore-forming age. A ^{40}Ar-^{39}Ar plateau age (195 ± 1.05 Ma) of quartz veinlets from the ores was obtained in Yangshan (Qi et al., 2005). Yang et al. (2006) used electron microprobe chemical technique on monazites from the Au-bearing granitic dikes to yield an isochron age of 190 ± 3 Ma. Dating for the intermediate-acid dikes (some of them are mineralized) within the Yangshan ore field obtained a Late Triassic age of 215–218 Ma (Lei et al., 2010; Sun et al., 2012; Yang et al., 2015b), which is consistent with the ages of the south Qinling granites (Sun et al., 2002a). Until the present study, the ore-forming age of the Yangshan gold deposits have not been established. Due to a lack of age confirmation between the mineralized phyllites and dikes, it is hard to say that the mineralized dikes truly represent the ore formation age in Yangshan. However, in view of the mineralized acid dikes, and the ore bodies near the dikes with high Au grades, it is suggested that the heat source which drove fluid-rock exchange and Au deposition most likely originates from a deep large intrusion which is expressed as the common dikes in the surface of Yangshan (Fig. 2). The Late Triassic dike age is proposed to represent magmatic event during extension after post-collision of Qinling orogen, which may associated closely with the formation of the Yangshan gold deposits (Qi et al., 2005; Yang et al., 2006).

A detailed comparison between Nevada's Carlin-type gold deposits and the Yangshan gold deposits (Table 5) shows that many similarities exist between them with some differences. For example, the Yangshan

Table 5
A comparison between Nevada's Carlin-type gold deposits and the Yangshan gold deposits.

Items	Gold deposits of Nevada	Gold deposits of Yangshan
Tectonic setting	Deformed and rifted North American cratonic margins with passive margin sequences dominated by carbonate rocks, and development of *syn*-sedimentary fault	Strongly deformed and rifted Yangtze cratonic margin with passive margin sequences dominantly by carbonate-bearing siliciclastic rocks
Ore-controlling structures	Regional Roberts Mountain Thrust and it's a series of secondary faults system, and structural culminations (e.g. doubly plunging anticline, domes)	Anchanghe-Guanyinba thrust fault as a branch of regional Mianlue suture zone and empty space of local anticline core
Ore-hosted terranes component	Carbonaceous silty limestone, dolomite with minor siliciclastic rocks	Calcareous silty sandstone, carbonaceous phyllite interlayered minor limestone
Deformation and metamorphism of host rock	Moderate deformation	Strong deformed and cataclastic host rock with low greenschist facies metamorphism
Deposits distribution	Occurring as clusters mainly in the lower plate of the Roberts Mountains thrust, near or within 100 m from the fault plane	Occurring as clusters along the high-angle (50–70 °C) Anchanghe-Guanyinba thrust fault zone with a variable width from tens of meters to several kilometers
Typical assemblage of ore minerals and gangue minerals	Arsenian pyrite, marcasite; jasperoid, drusy quartz, illite/kaolinite	Arsenian pyrite, arsenopyrite, stibnite; quartz, calcite, illite/kaolinite
Au occurrences	Invisible gold structurally bounded or as nano-particles in sulfides	Major invisible Au bounded in pyrite or arsenopyrite with minor visible Au in stibnite-quartz vein
Ore fluids	No-boiling ore fluids from 180 to 240 °C with low salinity (mostly ≤ 6 wt% Nacl eq.), and minor CO_2 (< 4 mol%)	Boiling ore fluids from 230 to 280 °C with low salinity (2.0–6.0 wt %), and abundant CO_2 (7.3–21.5 mol%)
Ore formation manner	Au deposition in sulfides accompanied by jasperoid replacement of carbonate minerals, alternation of silty rock components to illite and kaolinite, sulfidation of Fe in host rocks by ore fluids	Dominant invisible Au deposition by emplacement and microfissure–filling of ore fluids leading to overgrowth of sulfides with minor visible gold in stibnite-quartz vein at late extensional stage
Mineralization-related alteration	Decarbonatization, silicification, argillization, and sulfidation	Decarbonatization, silicification, argillization, and sulfidation
Lateral and vertical Zonation of mineral, element, and alternation	No lateral and vertical ore-related zonation	No lateral and vertical ore-related zonation
Paragenesis of ore-forming elements	Au-Tl-As-Hg-Sb(Te),with low Ag and base metal	Au-As-Sb, with minor Ag and base metal
Magmatic activity within ore field	Four magmatic episodes of Jurassic, Cretaceous, Eocene, and Miocene identified, of these, Eocene magma regarded as ore-related. And some of rhyolite dikes mineralized themselves	A series of Late Triassic intermediate-acid dikes development, of these, plagiogranite dikes mineralized reaching to ore grades
In-situ δ ^{34}S Characteristics of Au-carrying pyrite	$\delta^{34}S$ range of −1 to 4% by SIMS spot analyses of ore-related pyrite overgrowths indicating a magmatic sulfur source	$\delta^{34}S$ range of −7 to 1.3% by nanoSIMS spot analyses of ore-related pyrite overgrowths implying a magmatic sulfur. And similar Au, trace elements, and sulfur isotopic distribution pattern between Nevada and Yangshan
Cover development and denudation	Roberts Mountains allochthon consisting of fine-grained clastic rocks and chert emplaced during mid-Paleozoic as the first cover; Later Paleozoic to Mesozoic sedimentary rocks, and Cenozoic sediments as second cover; volcanic rhyolite rooted by deep intrusion reserved implying shallower denudation	Ore-hosting Middle Devonian strata exposed on the surface without any cover; granitic dikes cropping out indicating deeper denudation
Involvement of meteoric water for ore formation	Yes	Yes
Coeval magma-related mineralization, e.g. porphyry or skarn styles	No coeval porphyry mineralization documented	No coeval porphyry and skarn mineralization documented, but commonly developed Late Triassic dikes are likely coeval with gold mineralization
Proposed genetic style	Classic Carlin-type	Between Carlin-type and orogenic style

Notes: Data from references of Arehart et al., 2003; Cline et al., 2005, 2013; Liang et al., 2013, 2014; Ressel et al., 2000, 2006; Muntean et al., 2011; Li et al., 2007a; Kesler et al., 2005; Colgan et al., 2014; Yang et al., 2015a.

gold deposits have more non-reactive and strongly deformed host rocks, higher CO_2 content in the fluid, and higher ore formation temperatures than that in Nevada. This makes the Yangshan gold deposits look like more similar to orogenic style. In fact, CO_2 in the ore fluids may be derived mainly from the decomposition of the host rock driven by a magmatic heat source or strong compression during orogeny (De Paola et al., 2011), rather than water-rock interaction between acid ore fluids and the carbonate host rock. Therefore, the higher CO_2 content in the ore fluids of the Yangshan gold deposits can be attributed to the emplacement of the intrusions underlying the ore field, and the stronger deformation of the host rocks during the orogensis of the western Qinling during the Late Triassic.

6. Conclusions

Based on the data sets of microthermometry, He-Ar isotopes of fluid inclusions, multiple element mapping and in-situ sulfur isotopes of the Au-bearing arsenian pyrite, combined with previous ore mineralogy studies and detailed field observations, we characterized the nature and origin of ore fluids of the Yangshan gold deposits. The ore-forming fluid with abundant CO_2 displays typical features of orogenic gold deposit. Recycled meteoric water heated by a concealed deep magma heat source was likely involved into the Au mineralization. The in-situ sulfur isotope analyses reveal that the ore related sulfur sources are likely derived from deep magmatic sulfur likely contaminated by the sedimentary sulfur. The NanoSIMS elemental mapping combining with in situ sulfur isotopes distribution implies that the episodic magma-hydrothermal fluids bringing high As, Au and lighter S are more convincing to explain the characteristics of the pyrites. The overgrowth of the preexisting pyrites by the fluid should be responsible for the gold deposition. Therefore, multi-sourced fluids are likely involved in the formation of the Yangshan gold deposits, but a magmatic-hydrothermal fluid may play a key role. In summary, from deposit geology, ore fluids features to the micro characteristics of the Au-carrying sulfides, the Yangshan gold deposits displays features between Carlin-type and orogenic gold deposit. This work also suggests that NanoSIMS is a robust technique unlocking simultaneously gold states, distribution, ore fluids sources, and characterizing in detail the processes of ore formation.

Acknowledgments

First of all, we should thank the officers and soldiers of the 12th Gold Exploration Branch of Armed Police of P. R. China for their special access to entering into the Yangshan ore field for geological survey and sampling. We thank research fellow Xianren Ye of Laboratory of Gas Geochemistry, Lanzhou Institute of Geology, CAS, who help us analyze the noble gas isotopes of He and Ar. Thanks are given to the Raman Spectrometry Laboratory and Microthermometry Laboratory of the Sun Yat-Sen University for the vapour composition analysis and microthermometry of fluid inclusion. Electron Microbeam Analysis Laboratory in University of Science and Technology helped us complete BSE images of the pyrites. Special thanks are given to the Key Laboratory of Earth and Planetary Physics, Institute of Geology and Geophysics, CAS, for providing experiment hours of NanoSIMS elemental mapping and in situ sulfur isotopes analyses. We also thank the editors and anonymous reviewers for their constructive comments and suggestions about our manuscript. This work was jointly founded by the National Natural Science Foundation of China (No. 41273031), Taishan Scholar Special Project Funds (No. ts201511076), and Key Research and Development Project of Shandong Province (No. 2017CXGC1604).

References

Arehart, G.B., Chakurian, A.M., Tretbar, D.R., Christensen, J.N., Mcinnes, B.A., Donelick, R.A., 2003. Evaluation of radio isotope dating of Carlin-type deposits in the Great Basin, Western North America, and implications for deposit genesis. Econ. Geol. 98, 235–248.

Ballentine, C.J., 2002. Production, release and transport of noble gases in the continental crust. Rev. Mineral. Geochem. 47, 481–538.

Barker, S.L.L., Hickey, K.A., Cline, J.S., Dipple, G.M., Kilburn, M.R., Vaughan, J.R., Longo, A.A., 2009. Uncloaking invisible gold: Use of NanoSIMS to evaluate gold, trace elements, and sulfur isotopes in pyrite from Carlin-type gold deposits. Econ. Geol. 104, 897–904.

Bodnar, R.J., 1993. Revised equation and table for determining the freezing point depression of H_2O-Nacl solutions. Geochim. Cosmochim. Acta 57, 683–684.

Bruno, L.A., Baur, H., Graf, T., Schlüchter, C., Signer, P., Wieler, R., 1997. Dating of Sirius Group tillites in the Antarctic Dry Valleys with cosmogenic ^{3}He and ^{21}Ne. Earth Planet. Sci. Lett. 147, 37–54.

Burnard, P.G., Hu, R.Z., Turner, G., Bi, X.W., 1999. Mantle, crustal and atmospheric noble gases in Ailaoshan gold deposits, Yunnan Province, China. Geochim. Cosmochim. Acta 63, 1595–1604.

Chang, Z.S., Large, R.R., Maslennikov, V., 2008. Sulfur isotopes in sediment-hosted orogenic gold deposits: Evidence for an early timing and a seawater sulfur source. Geology 36, 971–974.

Chen, Y.J., Zhang, J., Zhang, F.X., Pirajno, F., Li, C., 2004. Carlin-type and Carlin-like gold deposits in western Qinling Mountains and their metallogenic time, tectonic setting and model. Geol. Rev. 50, 134–152 (in Chinese with English abstract).

Cline, J.S., Hofstra, A.H., Muntean, J.L., Tosdal, D., Hickey, K., 2005. Carlin-type gold deposits in Nevada: Critical geologic characteristics and viable models. Econ. Geol. 100th Anniversary Volume 451–484.

Cline, J.S., Muntean, J.L., Gu, X.X., Xia, Y., 2013. A comparison of Carlin-type gold deposits: Guizhou Province, Golden Triangle, Southwest China, and Northern Nevada, USA. Geosci. Front. 20, 1–18.

Colgan, J.P., Henry, C.D., John, D.A., 2014. Evidence for large-magnitude, post-Eocene extension in the Northern Shoshone Range, Nevada, and its implications for the structural setting of Carlin-Type gold deposits in the lower plate of the Roberts Mountains Allochthon. Econ. Geol. 109, 1843–1862.

Collins, P.L.F., 1979. Gas hydrates in CO_2-bearing fluid inclusions and the use of freezing data for estimation of salinity. Econ. Geol. 74, 1435–1444.

De Paola, N., Hirose, T., Mitchell, T., Toro, G.D., Viti, C., Shimamoto, T., 2011. Fault lubrication and earthquake propagation in thermally unstable rocks. Geology 39, 35–38.

Ding, D.J., Liang, J.L., Sun, W.D., Guo, J.H., Li, H., Ye, X.R., 2014. Ore genesis of the Yangshan gold deposit: Constrain from the He-Ar isotopic system of ore fluids. Bull. Mineral., Petrol. Geochem. 33, 813–819 (in Chinese with English abstract).

Dunai, T.J., Baur, H., 1995. Helium, neon, and argon systematics of the European subcontinental mantle: Implications for its geochemical evolution. Geochim. Cosmochim. Acta 59, 2767–2783.

Goldfarb, R.J., Groves, D.I., 2015. Orogenic gold: Common or evolving fluid and metal sources through time. Lithos 233, 2–26.

Goleby, B.R., Blewett, R.S., Korsch, R.J., Champion, D.C., Cassidy, K.F., Jones, L.E.A., Groenewald, P.B., Henson, P., 2004. Deep seismic reflection profiling in the Archaean northeastern Yilgarn craton, Western Australia: Implications for crustal architecture and mineral potential. Tectonophysics 388, 119–133.

Graham, D.W., 2002. Noble gas isotope geochemistry of mid-ocean ridge and ocean island basalts: Characterization of mantle source reservoirs. Rev. Mineral. Geochem. 47, 247–317.

Graupner, T., Niedermann, S., Kempe, U., Klemd, R., Bechtel, A., 2006. Origin of ore fluids in the Muruntau gold system: Constraints from noble gas, carbon isotope and halogen data. Geochim. Cosmochim. Acta 70, 5356–5370.

Groves, D.I., Goldfarb, R.J., Gebre-Mariam, M., Hagemann, S.G., Robert, F., 1998. Orogenic gold deposits: A proposed classification in the context of their crustal distribution and relationship to other gold deposit types. Ore Geol. Rev. 13, 7–27.

Hagemann, S.G., Gebre-Mariam, M., Groves, D.I., 1994. Surface-water influx in shallow-level Archean lode gold deposits in Western Australia. Geology 22, 1067–1070.

Heinrich, C.A., 2005. The physical and chemical evolution of low-salinity magmatic fluids at the porphyry to epithermal transition: a thermodynamic study. Miner. Deposita 39, 864–889.

Henry, C.D., Boden, D.R., 1998. Eocene magmatism: The heat source for Carlin-type gold deposits of northern Nevada. Geology 26, 1067–1070.

Hodkiewicz, P.F., Groves, D.I., Davidson, G.J., Weinberg, R.F., Hagemann, S.G., 2009. Influence of structural setting on sulphur isotopes in Archean orogenic gold deposits, Eastern Goldfields Province, Yilgarn, Western Australia. Miner. Deposita 44, 129–150.

Hofstra, A.H., Leventhal, J.S., Northrop, H.R., Landis, G.P., Rye, R.O., Birak, D.J., Dahl, A.R., 1991. Genesis of sediment-hosted disseminated gold deposits by fluid mixing and sulfidization: Chemical-reaction-path modeling of ore-depositional processes documented in the Jerritt Canyon district, Nevada. Geology 19, 36–40.

Hofstra, A.H., Cline, J.S., 2000. Characteristics and models for Carlin-type Au deposits. Rev. Econ. Geol. 13, 163–220.

Hou, L., Peng, H.J., Ding, J., Zhang, J.R., Zhu, S.B., Wu, S.Y., Wu, Y., Ouyang, H.G., 2016. Textures and in situ chemical and isotopic analyses of pyrite, Huijiabao Trend, Youjiang Basin, China: implications for paragenesis and source of sulfur. Econ. Geol. 111, 331–353.

Hronsky, J.M.A., Groves, D.I., Loucks, R.R., Begg, G.C., 2012. An unified model for gold mineralization in accretionary orogens and implications for regional scale exploration targeting methods. Miner. Deposita 47, 339–358.

Kendrick, M., Burgess, R., Pattrick, R., Turner, G., 2001. Fluid inclusion noble gas and halogen evidence on the origin of Cu-porphyry mineralising fluids. Geochim. Cosmochim. Acta 65, 2651–2668.

Kerrich, R., Goldfarb, R., Groves, D., Garwin, S., Jia, Y.F., 2000. The characteristics,

origins and geodynamic settings of supergiant Au metallogenic provinces. Sci. China (Series D) 43, 1–68.
Kesler, S.E., Fortuna, J., Ye, Z.J., Alt, J.C., Core, D.P., Zohar, P., Borhauer, J., Chryssoulis, S.L., 2003. Evaluation of the role of sulfidization in deposition of gold, Screamer Section of the Betze-Post Carlin-Type deposit, Nevada. Econ. Geol. 98, 1137–1157.
Kesler, S.E., Riciputi, L.C., Ye, Z.J., 2005. Evidence for a magmatic origin for Carlin-type gold deposits: isotopic composition of sulfur in the Betze-Post-Screamer deposit, Nevada, USA. Miner. Deposita 40, 127–136.
LaFlamme, C., Dennis, S., Nicolas, T., Stefano, C., Marco, F., Vikraman, S., Heejin, J., François, V., Martin, L., 2017. Multiple sulfur isotopes monitor fluid evolution of an orogenic gold deposit. Geochim. Cosmochim. Acta. https://doi.org/10.1016/j.gca.2017.11.003.
Large, R.R., Bull, S.W., Maslennikov, V.V., 2011. A carbonaceous sedimentary source-rock model for Carlin-Type and orogenic gold deposits. Econ. Geol. 106, 331–358.
Large, R.R., Danyushevsky, L., Hollit, C., Maslennikov, V., Meffre, S., Gilbert, S., Bull, S., Scott, R., Emsbo, P., Thomas, H., Singh, B., Foster, J., 2009. Gold and trace element zonation in pyrite using a laser imaging technique: Implications for the timing of gold in orogenic and Carlin-style sediment-hosted deposits. Econ. Geol. 104, 635–668.
Lei, S.B., Qi, J.Z., Chao, Y.Y., 2010. Zircon SHRIMP U-Pb ages of moderate-acid dykes and ore – forming epochs of Yangshan gold belt in Gansu Province. Miner. Deposits 29, 869–880 (in Chinese with English abstract).
Li, J., Chen, Y.J., Li, Q.Z., Lai, Y., Yang, R.S., Mao, S.D., 2007a. Fluid inclusion geochemistry and genetic type of the Yangshan gold deposit, Gansu, China. Acta Petrol. Sin. 23, 2144–2154 (in Chinese with English abstract).
Li, H.Y., Li, Y.J., Yuan, W.M., Yang, Q.R., Kang, G.L., Cao, J.F., 2007b. Mineral geochemistry in the Dashui diorite-type gold deposit, Gansu Province. Geol. Prospect. 43, 40–45 (in Chinese with English abstract).
Li, J.Z., Liu, H.B., Li, Y., Liu, D.L., Chen, Z.T., 2010. Ore-forming geological characteristics and prospecting direction of the Yangshan gold mineralization belt in Wen County, Gansu. Miner. Resour. Geol. 24, 193–197 (in Chinese with English abstract).
Li, N., Deng, J., Yang, L.Q., Goldfarb, R.J., Zhang, C., Marsh, E., Lei, S.B., Koenig, A.E., Lowers, H., 2014. Paragenesis and geochemistry of ore minerals in the epizonal gold deposits of the Yangshan gold belt, West Qinling, China. Miner. Deposita 49, 427–449.
Li, N., Yang, L.Q., Zhang, C., Zhang, J., Lei, S.B., Wang, H.T., Wang, H.W., Gao, X., 2012. Sulfur isotope characteristics of the Yangshan gold belt, West Qinling: constraints on ore-forming environment and material source. Acta Petrol. Sin. 28, 1577–1587 (in Chinese with English abstract).
Liang, J.L., Sun, W.D., Li, Y.L., Zhu, S.Y., Li, H., Liu, Y.L., Zhai, W., 2013. An XPS study on the valence states of arsenic in arsenian pyrite: Implications for Au deposition mechanism of the Yangshan Carlin-type gold deposit, western Qinling belt. J. Asian Earth Sci. 62, 363–372.
Liang, J.L., Sun, W.D., Zhu, S.Y., Li, H., Liu, Y.L., Zhai, W., 2014. Mineralogical study of sediment-hosted gold deposits in the Yangshan ore field, Western Qinling Orogen, Central China. J. Asian Earth Sci. 85, 40–52.
Lippolt, H.J., Weigel, E., 1988. ^{4}He diffusion in ^{40}Ar-retentive minerals. Geochim. Cosmochim. Acta 52, 1449–1458.
Liu, B.Z., Wang, J.P., Wang, K.X., Liu, J.J., Xie, H.Y., Cao, R.R., Hui, D.F., Cheng, J.J., 2011. Characteristics and geological significance of fluid inclusions in the Shuangwang gold deposit, Shanxi Province. Geoscience 25, 1088–1098 (in Chinese with English abstract).
Liu, C.H., Liu, J.J., Carranza, E.J.M., Yang, L.B., Wang, J.P., Zhai, D.G., Wang, Y.H., Wu, J., Dai, H.Z., 2016. Geological and geochemical constraints on the genesis of the Huachanggou gold deposit, western Qinling region, Central China. Ore Geol. Rev. 73, 354–373.
Liu, J.J., Liu, C.H., Carranza, E.J.M., Li, Y.J., Mao, Z.H., Wang, J.P., Wang, Y.H., Zhang, J., Zhai, D.G., Zhang, H.F., 2015a. Geological characteristics and ore-forming process of the gold deposits in the western Qinling region, China. J. Asian Earth Sci. 103, 40–69.
Liu, J.J., Dai, H.Z., Zhai, D.G., Wang, J.P., Wang, Y.H., Yang, L.B., Mao, G.J., Liu, X.H., Liao, Y.F., Yu, C., 2015b. Geological and geochemical characteristics and formation mechanisms of the Zhaishang Carlin-like type gold deposit, western Qinling Mountains, China. Ore Geol. Rev. 64, 273–298.
Loucks, R.R., Mavrogenes, J.A., 1999. Gold solubility in supercritical hydrothermal brines measured in synthetic fluid inclusions. Science 284, 2159–2163.
Ma, J., Lü, X.B., Escolme, A., Li, S., Zhao, N.L., Cao, X.F., Zhang, L.J., Lu, F., 2018. In-situ sulfur isotope analysis of pyrite from the Pangjiahe gold deposit: Implications for variable sulfur sources in the north and south gold belt of the South Qinling orogeny. Ore Geol. Rev. 98, 38–61.
Mao, J.W., Qiu, Y.M., Goldfarb, R.J., Zhang, Z.C., Garwin, S., Ren, F.S., 2002. Geology, distribution, and classification of gold deposits in the western Qinling belt, central China. Miner. Deposita 37, 352–377.
Mcdougall, I., Harrison, T.M., 1999. Geochronology and thermochronology by the ^{40}Ar/^{39}Ar method. Oxford University Press 34–59.
Meng, Q.R., Zhang, G.W., 2000. Geologic framework and tectonic evolution of the Qinling orogen, central China. Tectonophysics 323, 183–196.
Mernagh, T.P., Bastrakov, E.N., Zaw, K., Wygralak, A.S., Wyborn, L.A.I., 2007. Comparison of fluid inclusion data and mineralization processes for Australian orogenic gold and intrusion related gold systems. Acta Petrol. Sin. 23, 21–32.
Mueller, A.G., Hall, G.C., Nemchin, A.A., Stein, H.J., Creaser, R.A., Mason, D.R., 2008. Archaean high Mg monzodiorite syenite epidote skarn, and biotite sericite gold lodes in the Granny Smith-Wallaby district, Australia: U-Pb and Re-Os chronometry of two intrusion related hydrothermal systems. Miner. Deposita 43, 337–362.
Muntean, J.L., Cline, J.S., Simon, A.C., Longo, A.A., 2011. Magmatic hydrothermal origin of Nevada's Carlin-type Au deposits. Nat. Geosci. 4, 122–127.
Ohmoto, H., 1972. Systematics of sulfur and carbon isotopes in hydrothermal ore deposits. Econ. Geol. 67, 551–578.
Phillips, G.N., Groves, D.I., 1983. The nature of Archaean gold-bearing fluids as deduced from gold deposits of Western Australia. Geol. Soc. Aust. J. 30, 25–39.
Phillips, G.N., Powell, R., 2009. Formation of gold deposits: Review and evaluation of the continuum model. Earth-Sci. Rev. 94, 1–21.
Pitcairn, I.K., Teagle, D.A., Craw, D., Olivo, G.R., Kerrich, R., Brewer, T.S., 2006. Sources of metals and fluids in orogenic gold deposits: insights from the Otago and Alpine Schists, New Zealand. Econ. Geol. 101, 1525–1546.
Qi, J.Z., Li, L., Yuan, S.S., Liu, Z.J., Liu, D.Y., Wang, Y.B., Li, Z.H., 2005. A SHRIMP U-Pb chronological study of zircons from quartz veins of Yangshan gold deposit, Gansu Province. Miner. Deposits 24, 141–150 (in Chinese with English abstract).
Qian, D.Y., Xie, Y.L., Xu, J.H., 2003. Composition characteristics of fluid inclusions from Baguamiao gold deposit in Shanxi Province, China. J. Univ. Sci. Technol. Beijing 25, 1–4 (in Chinese with English abstract).
Qin, Y., Zhou, Z.J., 2009a. Organic geochemistry characteristics of Yangshan supperlarge gold deposit, Gansu Province. Acta Petrol. Sin. 25, 2801–2810 (in Chinese with English abstract).
Qin, Y., Zhou, Z.J., 2009b. Organic geochemistry characteristics of Yangshan super-large gold deposit, Gansu Province. Acta Petrol. Sin. 25, 2801–2810 (in Chinese with English abstract).
Ressel, M.W., Henry, C.D., 2006. Igneous geology of the Carlin Trend, Nevada: Development of the Eocene plutonic complex and significance for Carlin-Type gold deposits. Econ. Geol. 101, 347–383.
Ressel, M.W., Noble, D.C., Henry, C.D., Trudel, W.S., 2000. Dike-hosted ores of the Beast deposit and the importance of Eocene magmatism in gold mineralization of the Carlin Trend, Nevada. Econ. Geol. 95, 1417–1444.
Robert, F., 2001. Syenite associated disseminated gold deposits in the Abitibi greenstone belt, Canada. Miner. Deposita 36, 503–516.
Selvaraja, V., Caruso, S., Fiorentini, M.L., LaFlamme, C., Bui, T.H., 2017a. Atmospheric sulfur in the orogenic gold deposits of the Archaean Yilgarn Craton. Geology 45, 691–694.
Selvaraja, V., Fiorentini, M.L., Jeon, H., Savard, D.D., LaFlamme, C., Guagliardo, P., Caruso, S., Bui, T.H., 2017b. Evidence of local sourcing of sulfur and gold in an Archaean sediment hosted gold deposit. Ore Geol. Rev. 89, 909–930.
Stenger, D.P., Kesler, S.E., Peltonen, D.R., Tapper, C.J., 1998. Deposition of gold in Carlin-type deposits: The role of sulfidization and decarbonation at Twin Creeks, Nevada. Econ. Geol. 93, 201–215.
Stuart, F.M., Burnard, P.G., Taylor, R.P., Turner, G., 1995. Resolving mantle and crustal contributions to ancient hydrothermal fluids: He-Ar isotopes in fluid inclusions from Dae Hwa W-Mo mineralisation, South Korea. Geochim. Cosmochim. Acta 59, 4663–4673.
Sun, J., Wei, Q.R., Yang, Q.D., Wang, Z.J., Hao, W., Liang, Y.H., Zhang, X.Q., Wang, J.Y., 2012. LA-ICP-MS U-Pb dating and geochemistry of porphyric dykes at the south of Anba area, Yangshan gold belt. Geol. Sci. Technol. Inf. 31, 88–97 (in Chinese with English abstract).
Sun, W.D., Li, S.G., Chen, Y.D., Li, Y.J., 2002a. Timing of synorogenic granitoids in the South Qinling, Central China: Constraints on the evolution of the Qinling-Dabie orogenic belt. J. Geol. 110, 457–468.
Sun, W.D., Li, S.G., Sun, Y., Zhang, G.W., Li, Q.L., 2002b. Mid-paleozoic collision in the North Qinling: Sm–Nd, Rb–Sr and ^{40}Ar/^{39}Ar ages and their tectonic implications. J. Asian Earth Sci. 21, 69–76.
Tolstikhin, I.N., 1978. A review – Some recent advances in isotope geochemistry of light rare gases. Adv. Earth Planet. Sci. 3, 33–62.
Ushikubo, T., Williford, K.H., Farquhar, J., Johnston, D.T., Van Kranendonk, M.J., Valley, J.W., 2014. Development of in situ sulfur four-isotope analysis with multiple Faraday cup detectors by SIMS and application to pyrite grains in a Paleoproterozoic glaciogenic sandstone. Chem. Geol. 383, 86–99.
Wei, L.M., 2007. Preliminary study on the ore-forming fluids of Baguamiao gold deposit, Shanxi Province. Acta Petrol. Sin. 23, 2257–2262 (in Chinese with English abstract).
Xue, Y., Campbell, I., Ireland, T.R., Holden, P., Armstrong, R., 2013. No mass-independent S isotope fractionation in auriferous fluids supports a magmatic origin for Archean gold deposits. Geology 41, 791–794.
Yan, F.Z., Li, Z.Q., 2008. Yangshan gold deposit: The largest Carlin and Carlin-like type gold deposit in China. Acta Geol. Sin. 82, 804–810.
Yan, F.Z., Qi, J.Z., Guo, J.H., 2010. Geology and exploration of Yangshan gold Deposit in Gansu Province. Geological Publishing House, Beijing, China, pp. 66.
Yan, J., Hu, R.Z., Liu, S., Lin, Y.T., Zhang, J.C., Fu, S.L., 2018. NanoSIMS element mapping and sulfur isotopes analysis of Au-bearing pyrite from the Lannigou Carlin-type gold deposit in SW China: New insights into the origin and evolution of Au-bearing fluid. Ore Geol. Rev. 92, 29–41.
Yang, L.Q., Deng, J., Dilek, Y., Qiu, K.F., Ji, X.Z., Li, N., Taylor, R.D., Yu, J.Y., 2015a. Structure, geochronology, and petrogenesis of the Late Triassic Puziba granitoid dikes in the Mianlue suture zone, Qinling orogen, China. Geol. Soc. Am. Bull. 127, 1831–1854.
Yang, L.Q., Deng, J., Li, N., Zhang, C., Ji, X., Yu, J., 2016. Isotopic characteristics of gold deposits in the Yangshan gold belt, West Qinling, central China: Implications for fluid and metal sources and ore genesis. J. Geochem. Explor. 168, 103–118.
Yang, R.S., Chen, Y.J., Zhang, F.X., Li, Z.H., Mao, S.D., Liu, H.J., Zhao, C.H., 2006. Chemical Th-U-Pb ages of monazite from the Yangshan gold deposit, Gansu and their geologic and metallogenic implications. Acta Petrol. Sin. 22, 2603–2610 (in Chinese with English abstract).
Yang, T., Zhu, L.M., Zhang, G.W., Wang, F., Lu, R.K., Xia, J.C., Zhang, Y.Q., 2012. Geological and geochemical constraints on genesis of the Liziyuan gold dominated polymetal deposit, western Qinling region, central China. Int. Geol. Rev. 54, 1944–1966.
Yang, W., Hu, S., Zhang, J.C., Hao, J.L., Lin, Y.T., 2015b. NanoSIMS analytical technique

and its applications in earth sciences. Sci. China Earth Sci. 58, 1758–1767.
Ye, X.R., Wu, M.B., Sun, M.L., 2001. Determination of the noble gas isotopic composition in rocks and minerals by mass spectrometry. Rock Miner. Anal. 20 (3), 174–178 (in Chinese with English abstract).
Yue, L.X., Yang, G.X., Wang, Y.M., Liu, X.H., 2013. Comprehensive information prospecting model of the Zhaishang gold deposit in Gansu Province. Gold Sci. Technol. 21, 43–47 (in Chinese with English abstract).
Zhai, W., Sun, X.M., Sun, W.D., Su, L.W., He, X.P., Wu, Y.L., 2009. Geology, geochemistry, and genesis of Axi: A Plaeozoic low-sulfidization type epithermal gold deposit in Xinjiang, China. Ore Geol. Rev. 36, 265–281.
Zhang, Z.A., 1993. A study of mineral inclusion and stable isotope from Laerma gold deposit. J. Mineral. Petrol. 13, 50–58 (in Chinese with English abstract).
Zhang, F.X., Chen, Y.J., Li, C., Zhang, J., Ma, J.Q., Li, X., 2000. Geological and geochemical character and genesis of the Jinlongshan-Qiuling gold deposits in Qinling orogen: Metallogenic mechanism of the Qinling-pattern Carlin-type gold deposits. Sci. China (Series D) 43 (Supple), 95–107 (in Chinese with English abstract).
Zhang, J., Chen, Y.J., Zhang, F.X., Li, C., 2002a. Geochemical study of ore fluid in Jinlongshan Carlin-type gold ore belt in southwestern Shanxi Province. Miner. Deposits 21, 283–291 (in Chinese with English abstract).
Zhang, F.X., Zhang, J., 2003a. Geological-geochemical characteristics of Carlin- type and Carlin-like- gold deposits in South Qinling Mountains. Acta Geochimica 22, 11–22.
Zhang, G.W., Dong, Y.P., Lai, S.C., Guo, A.L., Meng, Q.R., Liu, S.F., Cheng, S.Y., 2004a. Mianlue tectonic zone and Mianlue suture zone on southern margin of Qinling-Dabie orogenic belt. Sci. China (Series D-Earth Sciences) 47, 300–316.
Zhang, J.C., Lin, Y.T., Yan, J., Li, J.X., Yang, W., 2017. Simultaneous determination of sulfur isotopes and trace elements in pyrite with a NanoSIMS 50L. Anal. Method 9, 6653–6661.
Zhang, J.C., Lin, Y.T., Yang, W., Shen, W.J., Hao, J.L., Hu, S., Cao, M.J., 2014. Improved precision and spatial resolution of sulfur isotope analysis using NanoSIMS. J. Anal. At. Spectrom. 29, 1934–1943.
Zhang, X.C., Spiro, B., Halls, C.J., Stanley, C., Yang, K.Y., 2003. Sediment-hosted disseminated gold deposits in Southwest Guizhou, PRC: Their geological setting and origin in relation to mineralogical, fluid inclusion, and stable isotope characteristics. Int. Geol. Rev. 45, 407–470.
Zhang, Z.H., Ma, J.Q., Wang, Y., 2002b. Fluid inclusion characteristics of Jinshan gold deposit in West Qinling district and its geological significance. Miner. Deposits 21, 1106–1109 (in Chinese with English abstract).
Zhang, Z.H., Mao, J.W., Wang, Y., 2004b. Characteristics of fluid inclusions in the gold deposits within Zhongchuan area, western Qinling and their geological significance. Acta Petrol. Mineral. 23, 147–157 (in Chinese with English abstract).
Zhang, F.X., Zhang, J., 2003b. Geological-geochemical characteristics of Carlin- and Carlin-Like-Type gold deposits in South Qinling Mountains. Acta Geochimica 22, 11–22.
Zhao, J., Liang, J.L., Ni, S.J., Xiang, Q.R., 2016. In situ sulfur isotope composition analysis of Au-bearing pyrites using Nano-SIMS in Yangshan gold deposit, Gansu Province. Miner. Deposits 35, 653–662 (in Chinese with English abstract).
Zhao, J., Liang, J.L., Long, X.P., Li, J., Xiang, Q.R., Zhang, J.C., Hao, J.L., 2018. Genesis and evolution of framboidal pyrite and its implications for the ore-forming process of Carlin-style gold deposits, southwestern China. Ore Geol. Rev. 102, 426–436.
Zhu, L.M., Zhang, G.W., Li, B., Kang, L., Lu, S.L., 2009. Geology, isotope geochemistry and ore genesis of the Maanqiao gold deposit, Shanxi Province. Acta Petrol. Sin. 25, 431–443 (in Chinese with English abstract).
Zhu, M.T., Zhang, L.C., Wu, G., He, H.Y., Cui, M.L., 2013. Fluid inclusions and He-Ar isotopes in pyrite from the Yinjiagou deposit in the southern margin of the North China Craton: a mantle connection for poly-metallic mineralization. Chem. Geol. 351, 1–14.
Zhu, Y.N., Peng, J.T., 2015. Infrared microthermometric and noble gas isotope study of fluid inclusions in ore minerals at the Woxi orogenic Au-Sb-W deposit, western Hunan, South China. Ore Geol. Rev. 65, 55–69.